ADVANCED FUNCTIONAL MATERIALS
www.afm-journal.de

Layer-Based Heterostructured Cathodes for Lithium-Ion and Sodium-Ion Batteries

*Ya-Ping Deng, Zhen-Guo Wu, Ruilin Liang, Yi Jiang, Dan Luo, Aiping Yu, and Zhongwei Chen**

A critical bottleneck that hinders major performance improvement in lithium-ion and sodium-ion batteries is the inferior electrochemical activity of their cathode materials. While significant research progresses have been made, conventional single-phase cathodes are still limited by intrinsic deficiencies such as low reversible capacity, enormous initial capacity loss, rapid capacity decay, and poor rate capability. In the past decade, layer-based heterostructured cathodes acquired by combining multiple crystalline phases have emerged as candidates with a huge potential to realize performance breakthrough. Herein, recent studies on the structural properties, electrochemical behaviors, and synthesis route optimizations of these heterostructured cathodes are summarized for in-depth discussions. Particular attention is paid to the latest mechanism discoveries and performance achievements. This review thus aims to promote a deeper understanding of the correlation between the crystal structure of cathodes and their electrochemical behavior, and offers guidance to design advance cathode materials from the aspect of crystal structure engineering.

1. Introduction

With the rapid approach of climate change and fossil fuel reserves shortage, there is an urgent demand for efficient conversion and storage systems for renewable energy. The launch of Li-ion batteries (LIBs) in 1991 was a significant step toward reaching the goal of eliminating the reliance of the energy system on fossil fuels,[1–3] but major performance breakthroughs are still required for the battery technologies to truly satisfy the requirement of electric vehicles and grid storages. Admittedly, other energy storage technologies, including fuel cell, metal–air, and metal–sulfur batteries, have drawn in growing research attentions as possible alternative of LIBs with higher energy density.[3–12] However, these systems are limited by either intrinsic or economic barriers, and are still in the early stages of development and commercialization. As such, LIBs and the rapidly growing sodium-ion batteries (SIBs) with mature technology and competitive cost will likely continue to dominate key markets of energy storage systems in the near future.

The working principles of LIBs and SIBs are both based on intercalation electrochemistry. During charging, Li^+ or Na^+ deintercalate from the cathode and diffuse through Li/Na-salt containing aprotic electrolyte to the anode. The reverse process occurs during discharge and the electricity is produced via intercalation of Li^+/Na^+ into electrode materials.[13,14] Throughout this process, solid state diffusion of Li^+/Na^+ within the electrodes is the rate-limiting process that determines the output energy density of the batteries.[15] In the past 30 years, immense improvements have been achieved on the anode end, especially for carbon and alloy based materials.[16–22] In comparison, despite tremendous research interests from the USA, Korea, Japan, and China, conventional single-phase cathode materials (layered, spinel, or olivine) are yet to achieve a major leap in performance.[23–25] Hence, exploring high-performance cathode is the key to substantially improve the capabilities of LIBs and SIBs.

Crystal structural properties are known to heavily influence electrochemical behavior of cathode materials, and it has been discovered that rational modification of crystal structure can be utilized to optimize performance of LIBs and SIBs.[26] Recently, cathode materials with layer-based heterostructures are emerging as alternative candidates for next-generation LIBs/SIBs owing to their balanced overall electrochemical parameters in reversible capacity, initial coulombic efficiency, cyclic and rate performance. For example, when served as cathode for LIBs, the solid solutions of $R\bar{3}m$ $LiMO_2$ (M represents transition metal ions of Mn, Ni, Co, etc.) and $C2/m$ Li_2MnO_3 demonstrate discharge capacity as high as 350 mAh g^{-1} within the voltage window of 2.0 and 4.8 V (vs Li/Li^+), which is almost two times the values of conventional LIB cathodes.[27–29] Initial coulombic efficiency and cyclability of the resulting materials are also optimized in comparison to the $C2/m$ component.[30] Another example in SIBs is the P2–O3 integrated composite cathode, whose rate and cyclic performance are superior to pure O3-cathodes, while its initial coulombic efficiency and reversible capacity are improved when compared to pure P2-cathodes.[31]

Y. P. Deng, R. Liang, Dr. Y. Jiang, D. Luo, Prof. A. Yu, Prof. Z. Chen
Department of Chemical Engineering
Waterloo Institute for Nanotechnology
University of Waterloo
Waterloo, ON N2L 3G1, Canada
E-mail: zhwchen@uwaterloo.ca
Dr. Z. G. Wu
College of Chemical Engineering
Sichuan University
Chengdu 610065, China
The ORCID identification number(s) for the author(s) of this article can be found under https://doi.org/10.1002/adfm.201808522.

DOI: 10.1002/adfm.201808522

© 2019 WILEY-VCH Verlag GmbH & Co. KGaA, Weinheim

It is beyond our goal to present an exhaustive review on each family of the single-phase cathodes, but rather to provide a practical database with clear classification of heterostructured cathodes and in-depth analysis on the "structure–performance" relationship. As a representative of the widely investigated structure, layer-based heterostructured cathodes with superior performance are selected as the main material platform to elucidate the concerned issues. A concise overview on crystal configuration and corresponding Li^+/Na^+ diffusion manners of each conventional single-phase structures is first provided as fundamentals for discussion. Thereafter, the heterostructured cathodes are divided into categories, and representative works in each category are presented for systematic investigations. Historic evolutions, electrochemistry, latest progresses, and challenges of these multi-phase cathodes are also discussed, with focuses placed on the construction and adjustment of heterostructure, the synergy mechanism, and the corresponding influence on performance. Based on the insights acquired by studying the achievements of heterostructured cathodes, perspectives are provided as guidance for future efforts on developing advance cathodes through composite structure engineering.

2. LIBs

2.1. Single-Phase Cathode

2.1.1. $R\bar{3}m$-Layered Structure

The layered $LiMO_2$ are the earliest and most widely commercialized cathode materials for LIBs.[32] They typically exhibit a working plateau at 3.8 V (vs Li/Li^+) and a discharge capacity of around 200 mAh g^{-1}.[33] As demonstrated in **Figure 1**a, the crystallographic configuration of layered $LiMO_2$ is arrayed in rhombohedral ($R\bar{3}m$) α-$NaFeO_2$ symmetry with alternate Li and M layers formed by edge sharing octahedral unit cells.[34,35] The close-packed orientation of the MO_6 octahedrons in the M layers obstructs vertical diffusion of Li^+ along the *c* axis, which is responsible for the comparatively low Li^+ diffusion coefficients of layered materials (10^{-9}–10^{-10} cm^2 s^{-1}).[36] Moreover, site replacements between Li^+ and Ni^{2+} are also common in Ni-containing $LiMO_2$, as the Ni^{2+} and Li^+ ions have similar ionic radius.[37] This undesirable cation mixing would narrow the Li-layer space, which accelerates performance and structure deteriorations.[37,38]

2.1.2. C2/m-Layered Structure

Monoclinic *C*2/*m* layered Li_2MnO_3 (or $Li[Li_{1/3}Mn_{2/3}]O_2$) presents a α-$NaFeO_2$ symmetry similar to $LiMO_2$ (Figure 1b), except that the M layers are replaced by Li–Mn layers comprised of tetravalent manganese and monovalent lithium.[30] Previously, due to the nature of tetravalent manganese and its limited favorability for Li^+ intercalation, Li_2MnO_3 was considered by many to be electrochemically inert. This belief was proven false in 1999, when Li^+ extraction was demonstrated on the cathode material without oxidation of Mn^{4+}.[30,39] The most commonly accepted electrochemical behavior of Li_2MnO_3 involves the simultaneous extraction of Li^+ and O^{2+} at 4.5 V in the initial charging process, which gives a high theoretical capacity of 458 mAh g^{-1} for extracting two moles of Li^+.[28,40] However, this initial delithiation process also leads to irreversible structural evolution, which results in low initial coulombic efficiency and rechargeability.[41] The crystalogical transformation begins with the migration of Mn^{4+} from the Li–Mn layers into the Li layers, accompanied by the release of lattice O. It is then followed by compositional transformation of the material to MnO_2.[42] Upon relithiation, layered $LiMnO_2$ and spinel $LiMn_2O_4$ were found to be the main species instead of the

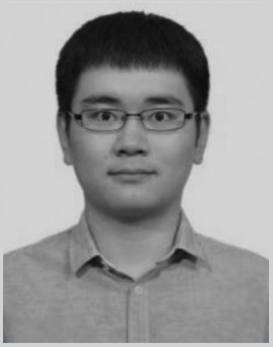

Ya-Ping Deng received his Master's degree (2016) in Xiamen University with Prof. Shi-Gang Sun. He is now pursuing his Ph.D. in chemical engineering under the supervision of Prof. Zhongwei Chen at the University of Waterloo. His research is currently focused on the exploration of novel electrode materials and solid-state electrolytes for lithium-ion batteries and rechargeable metal–air batteries.

Zhen-Guo Wu obtained his Ph.D. (2016) from the Sichuan University with Prof. Ben-He Zhong. He is currently an associate researcher at Sichuan University. His research interests include the development of advanced energy materials for lithium-ion and sodium-ion batteries.

Zhongwei Chen obtained his Ph.D. (2007) from the University of California, Riverside. He is a Canada Research Chair Professor (Tier 1) in Advanced Materials for Clean Energy at the University of Waterloo, a fellow of the Canadian Academy of Engineering, and the Vice President of the International Academy of Electrochemical Energy Science (IAOEES). His research interests involve the development of advanced energy materials and electrodes for fuel cells, metal–air batteries, and lithium-ion batteries.

 © 2019 WILEY-VCH Verlag GmbH & Co. KGaA, Weinheim

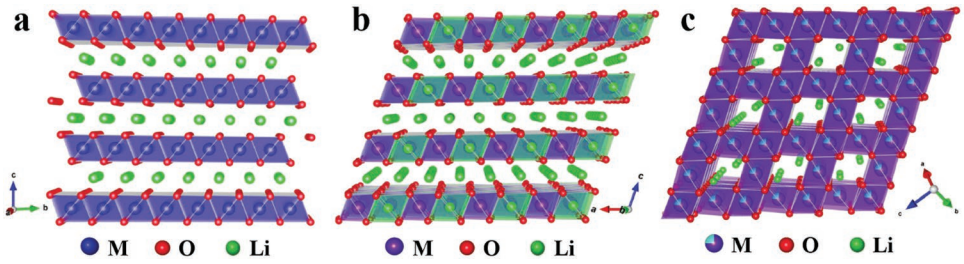

Figure 1. Crystalline structure of a) $R\bar{3}m$ trigonal layer; b) $C2/m$ monoclinic layer; c) $Fd\bar{3}m$ cubic spinel. Reproduced with permission.[26] Copyright 2018, Wiley-VCH.

original Li_2MnO_3.[40] As a result of this irreversible process, the lithiation–delithiation mechanism in the subsequent cycles is changed to the lower valence redox couple of Mn^{2+}/Mn^{3+} with fast voltage and capacity fading.[26,43]

2.1.3. $Fd\bar{3}m$ Spinel Structure

Since spinel oxides were introduced as cathode materials in 1983, their 3D Li^+ diffusion channels have attracted immense interest for applications in high-rate LIBs.[23,44,45] The cubic symmetry of $Fd\bar{3}m$ spinels with a general formula of $LiMn_2O_4$ is indicated in Figure 1c, where M cations and Li^+ occupy half of 16d octahedral sites and 8a tetrahedral sites, respectively.[45,46] These distributions establish 3D Li^+ diffusion pathways via the edge-sharing interconnection of 8a sites and their surrounding octahedral 16c sites.[47] The primary redox couple for $LiMn_2O_4$ is the Mn^{3+}/Mn^{4+} voltage plateau that locates at around 4.0 V. While the Mn^{2+}/Mn^{3+} plateau at about 3.0 V associated with Li^+ insertion to empty 16c octahedral sites and formation of $Li_2Mn_2O_4$ has also been reported.[2,48] For these Mn-based spinels, the main cause of capacity loss is the Jahn–Teller effect, which triggers the disproportion reaction of Mn^{3+} that generates Mn^{2+} and Mn^{4+}, followed by dissolution of Mn^{2+} to the electrolyte.[49] Targeted substitution with other cations, such as Ni^{2+}, Li^+, Mg^{2+}, Al^{3+}, Co^{2+}, etc., to raise average metal ion oxidation state to above 3.5 is a proven strategy that addresses the above issue and increases material specific capacity.[47,50] For example, with the substitution of Ni^{2+}, the spinel $LiNi_{0.5}Mn_{1.5}O_4$ exhibits an additional plateau at 4.7 V representing the redox of Ni^{2+}/Ni^{4+} with lithiation/delithiation at 8a tetrahedra.[51] Another typical $Fd\bar{3}m$ spinel member of this category is $Li_4Mn_5O_{12}$ (or $Li[Mn_{1.67}Li_{0.33}]O_4$), whose Mn is partially substituted by Li^+ and the remaining Mn is controlled to be tetravalent. This would eliminate the aforementioned 4.0 V plateaus, and the Li^+ insertion/extraction occurring at 3.0 V will be the sole electrochemical reaction of the material.[47,52] Nevertheless, applications of these spinel oxides in LIBs remain to be limited as their low practical capacity (150 mAh g^{-1}) restricts their energy storage capability.

2.2. Developing Layer-Based Heterostructured Cathode for LIBs

Different modification strategies on these traditional cathode materials were experimented to enhance their performance. First, following the development of nanoscience and nanotechnology, morphological designs for cathode materials have been widely explored to optimize the rate-limiting Li^+ diffusion kinetics.[33] Synthetic processes were reported in recent years to obtain architectures varying from zero to three dimensions, such as nanoparticles, nanowires, nanobricks, microcubes, microspheres, etc.[53–58] Two main objectives in these morphology targeted strategies are shortening Li^+ diffusion pathways and promoting electrolyte penetration.[59] Second, offering additional redox couples through compositional alteration to increase output capacity is another commonly reported method, e.g., the aforementioned alteration of Ni content in $R\bar{3}m$ layered and $Fd\bar{3}m$ spinel cathodes.[2,50,60] Third, rational modifications on crystal structure, such as heteroatom doping, have also been proven feasible. Taking Na doping as an example, Na^+ dopants can be used to expand crystal structure and widen the Li^+ diffusion channels due to larger ionic radius, which improves rate capability of Na^+ doped cathodes.[61–63] Last but not least, tuning crystal habit to increase the percentage of exposed (010) facets in $R\bar{3}m$ $LiMO_2$ has also been investigated to promote Li^+ diffusion.[53,64]

Despite these extensive research efforts on single-phase cathodes, their intrinsic performance ceiling is still too low for the increasing requirement of LIBs. An alternative approach for performance upgrade is to explore heterostructured composites that inherit merits of different crystal structures. These layer-based heterostructured LIB cathodes can be generally classified into three categories: $R\bar{3}m$–$C2/m$, $R\bar{3}m$–$Fd\bar{3}m$, and $R\bar{3}m$–$C2/m$–$Fd\bar{3}m$. Their structural features, functional mechanism, electrochemical behavior, and recent research progresses are presented separately in the following sections. Majority of the emphasis will be paid to the ternary $R\bar{3}m$–$C2/m$–$Fd\bar{3}m$ category due to its superior performance and relative recency.

2.2.1. $R\bar{3}m$–$Fd\bar{3}m$ (LS) Category

As discussed previously, the insufficient rate capability of $R\bar{3}m$ $LiMO_2$ mainly originates from its hindered Li^+ movements within the 2D diffusion planes, which has been a major challenge in its commercialization. One feasible approach of removing this blockade is to obtain $R\bar{3}m$–$Fd\bar{3}m$ (LS) heterostructured cathode by incorporating the $R\bar{3}m$ phase with $Fd\bar{3}m$ spinel, which utilizes the 3D diffusion channels available within the $Fd\bar{3}m$ spinels to accelerate Li^+

© 2019 WILEY-VCH Verlag GmbH & Co. KGaA, Weinheim

solid-state diffusion. Based on this concept, a polyvinylpyrrolidone (PVP) involved post-treatment strategy was reported by Cho et al. to assemble a core–shell structured LS cathode marked as HS–$LiNi_{0.54}Co_{0.12}Mn_{0.34}O_2$ (**Figure 2**a).[65] For a typical particle, the core was $Li[Ni_{0.54}Co_{0.12}Mn_{0.34}]O_2$ with $R\bar{3}m$ phase, while the shell was observed by transmission electron microscopy (TEM) to be $Fd\bar{3}m$ $Li_{1+x}[CoNi_xMn_{2-x}]_2O_4$ with a thickness less than 0.5 µm (Figure 2b). After 15 cycles of rate capability test at 60 °C, this heterostructured cathode yields a capacity of 142 mAh g^{-1} at 0.2 C that is higher than the two single phase materials between 3.0 and 4.5 V (Figure 2e). The highly stable $Fd\bar{3}m$ shell also benefits the electrochemical stability as the material maintains 95% of its initial capacity after 40 cycles at 0.5 C (Figure 2f). Similarly, Liu and co-workers also fabricated LS composite (referred as SC-LNCMO) with layered $LiNi_{0.8}Co_{0.1}Mn_{0.1}O_2$ as core and spinel $LiNi_xCo_yMn_{2-x-y}O_4$ as shell (Figure 2c,d).[66] When compared to the single phase references, this composite demonstrates a capacity improvement of 98 mAh g^{-1} in cyclic test at 10 C, and retains 50% more capacity after 100 cycles at 0.1 C (Figure 2g,h). Indeed, the reversible capacities of the presented composites are still limited to about 200 mAh g^{-1} at 0.1 C rate, but the positive reinforcement of $Fd\bar{3}m$ spinels on rate performance and cyclability of $R\bar{3}m$ $LiMO_2$ can be clearly observed.[65–68]

2.2.2. $R\bar{3}m$–$C2/m$ (LL) Category

The concept of combining $R\bar{3}m$ layered $LiMO_2$ with $C2/m$ layered Li_2MnO_3 was first reported and realized by Koichi et al.[72] As presented in previous section, both $R\bar{3}m$ $LiMO_2$ and $C2/m$ Li_2MnO_3 exhibit the α-$NaFeO_2$ symmetry. Therefore, atomic integration between the two components is possible to produce solid solution of $LiMO_2 \cdot Li_2MnO_3$ (LL), or Li-rich materials with a general formula of $Li(Li_xMn_yCo_zNi_{1-x-y-z})O_2$.[30,73] The presence of Li_2MnO_3 in LL is commonly reflected in X-ray diffraction (XRD) pattern with superlattice diffraction peaks between 20° and 23°.[74] For electrochemical process under the voltage of 4.4 V, Li_2MnO_3 acts as a structural stabilizer in LL.[75] When the voltage window is expanded between 2.0 and 4.8 V, Li_2MnO_3 transforms to a Li^+ reservoir to offer additional capacity.[76] As a result, LL is capable of delivering ultrahigh capacities over 300 mAh g^{-1}, turning it into a research hot spot in the last decade.

However, LL is still far from practically feasible, as it suffers from several inherent problems, including huge initial capacity loss, poor cyclability, and inferior rate capability.[41,42,77–86] Great efforts have been expended to address these drawbacks, some common methods include synthetic process optimization,[87–91] heteroatom doping,[92–95] and surface treatment.[96–108] For example, anion doping (such as F^-) and compositing with lithium-free insertion hosts (MnO_3, V_2O_5, etc.) are both effective ways to reduce the initial capacity loss (**Figure 3**a,b).[69,70,109–113] LL synthesized under solvothermal condition proposed by Sun and co-workers also exhibits much higher specific capacity and capacity retention than ones obtained through conventional coprecipitation (Figure 3c).[71,114] Na^+ doping also shows positive effects on boosting rate capability of LL by widening its 2D Li^+ diffusion planes (Figure 3d), which has a similar mechanism to elemental dopants with larger ionic radius.[61,62,115]

Voltage fading of LL is commonly accepted to be correlated with the layered-to-spinel structural transformation during electrochemical cycling, and it is often reflected by the gradual appearance of a voltage plateau at 3.0 V.[78,84,119–121] Thereafter, the voltage fading is further accelerated by element dissolution and surface corrosion of hydrofluoric acid (HF) generated through side reactions between $LiPF_6$ containing electrolyte and oxygen radicals (**Figure 4**a).[42,116,122,123] These phenomena also cause sharp decrease in capacity and energy density. In present scenarios, replacing polyvinylidene fluoride (PVDF) with novel binder that shields the active material surface is found to be a facile but effective approach to counter the voltage fading.[124] Several water-soluble binders have been tested with LL cathodes in LIB fabrication. In one example, sodium carboxymethyl cellulose (CMC) was introduced by Pan and co-workers as a novel binder in $Li_{1.2}Ni_{0.13}Co_{0.13}Mn_{0.54}O_2$.[117] The cell with CMC binder delivers a midpoint voltage retention of 88% after 100 cycles of charge and discharge at 20 mA g^{-1} (Figure 4b), which is significantly better than cells prepared with PVDF (74%) or polyacrylonitrile (PAN, 76%); its capacity retention is also the best among the three electrodes. The effects of CMC on suppressing voltage and capacity fading can be attributed to two aspects. The first is its strong adhesiveness that suppresses element dissolution and material detachment. The second function is summarized by the Li^+/Na^+ ion-exchange mechanism that describes the occupation of Na^+ from CMC at Li^+ vacancies after delithiation, which hinders undesirable migration of M cations into the Li-layers that eventually causes structure collapse (inset of Figure 4b).[117] In another example, uniform and tight coating of Guar gum on LL was reported to effectively stabilize the elemental distribution and inhibit the electrolyte corrosion. As a result, the voltage fading of the cathode material is largely suppressed with its voltage retention increasing from 62.4% to 95.2% (Figure 4c–e).[118] Recently, Ba^{2+} or Al^{3+} modified sodium alginate binders were also reported to exhibit positive influences on electrochemical behavior of LL.[125]

Another typical approach to counter voltage fading with LL is surface modification. Liu and co-workers demonstrated that $LiFePO_4$ coating layer on LL can confine the migration of transition metals and stabilize lattice structure.[126] The charge and discharge curves of 5 wt% $LiFePO_4$ coated $Li_{1.2}Ni_{0.13}Co_{0.13}Mn_{0.54}O_2$ are provided in **Figure 5**a. As shown, voltage fading in the reported material is almost negligible. More importantly, the original layered crystal structure is retained after 120 cycles (Figure 5b). Li–Mg–PO_4 protective layer on the surface of $Li_{1.17}Ni_{0.17}Co_{0.17}Mn_{0.5}O_2$ was also reported to positively affect the material cyclic stability. The improvements were attributed to the proposed "pillar effect," which describes the presence of Mg^{2+} in Li layers suppressing transition metal migration.[127] Additionally, it was discovered that finely designed composition adjustment of LL, such as altering Ni to Mn ratio[34,81] and optimized substitution of Al,[128] Ru,[78] Ir,[129,130] Y,[131] Ti,[94] Zr,[132] etc., can impact the electrochemical performance positively. These strategies aim to stabilize the layered structure of LL and prevent the Jahn–Teller effects by reducing the Mn ratio, so that the degree of

© 2019 WILEY-VCH Verlag GmbH & Co. KGaA, Weinheim

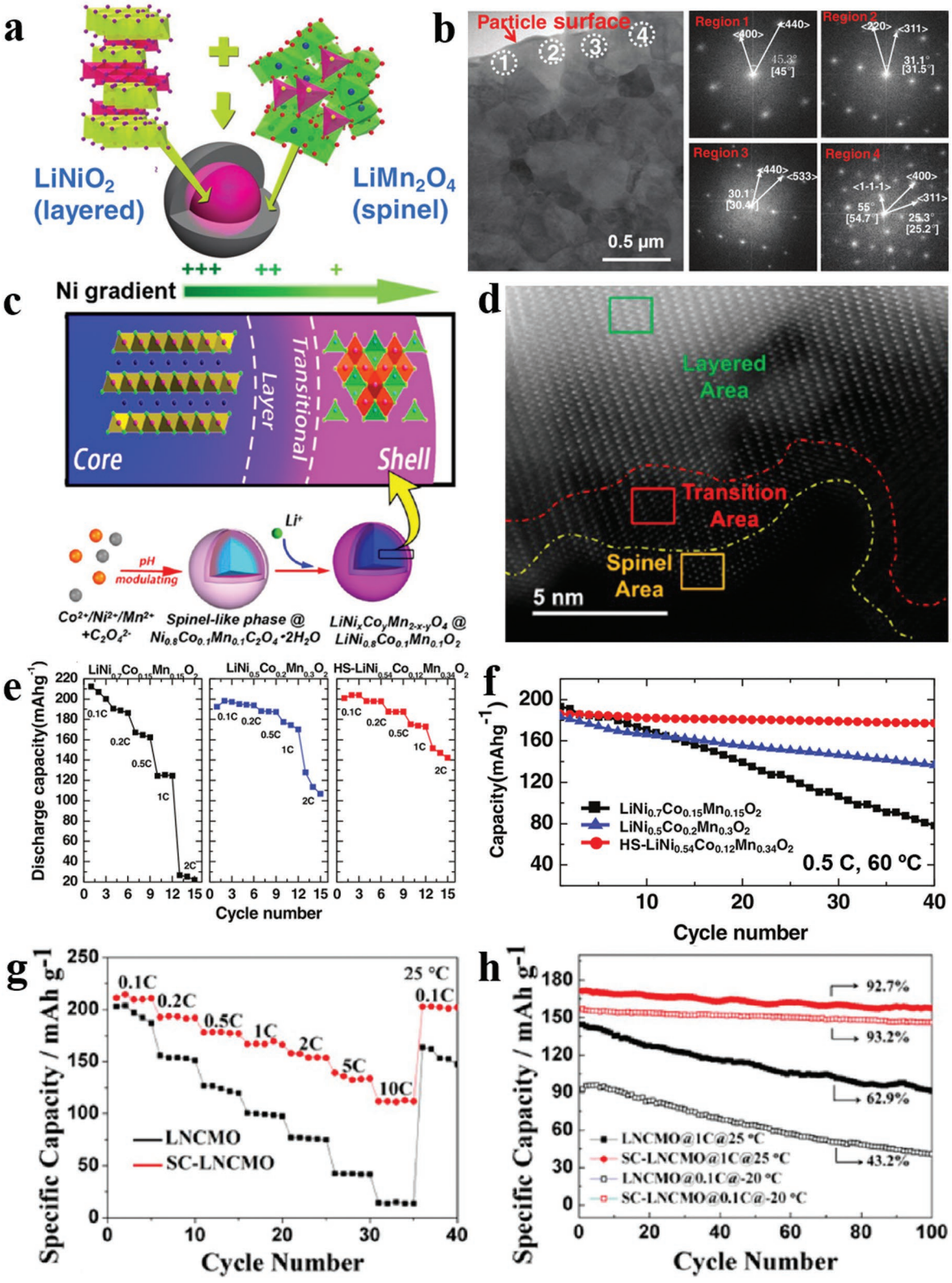

Figure 2. a) Schematic diagram, b) transmission electron microscopy (TEM) image of the cross-sectioned particle and digitalized Fourier transformed images at the corresponding regions. e,f) Performance comparison of HS-$LiNi_{0.54}Co_{0.12}Mn_{0.34}O_2$, $LiNi_{0.5}Co_{0.2}Mn_{0.3}O_2$, and $LiNi_{0.7}Co_{0.15}Mn_{0.15}O_2$. Reproduced with permission.[65] Copyright 2014, Wiley-VCH. c) Schematic diagrams, d) high-resolution TEM (HRTEM) image, g) rate, and h) cyclic performance of LS heterostructured cathode (SC-LNCMO) and layered materials (LNCMO). Reproduced with permission.[66] Copyright 2014, American Chemical Society.

© 2019 WILEY-VCH Verlag GmbH & Co. KGaA, Weinheim

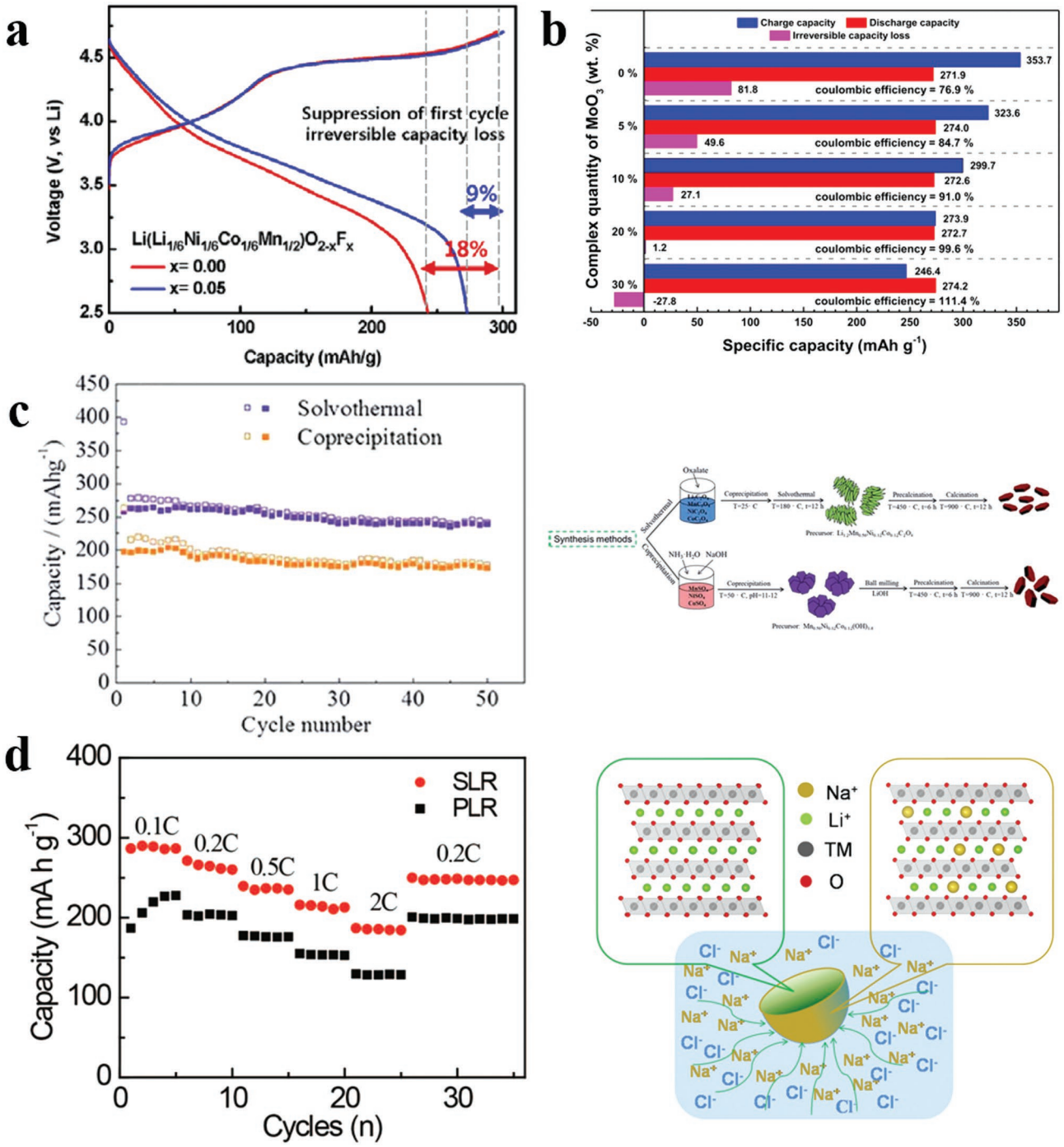

Figure 3. a) Initial charge and discharge profiles of $Li(Li_{1/6}Ni_{1/6}Co_{1/6}Mn_{1/2})O_{2-x}F_x$ ($x = 0.00$ or 0.05) at 0.1 C between 2.5 and 4.8 V. Reproduced with permission.[69] Copyright 2016, Elsevier. b) Charge capacity, discharge capacity, and irreversible capacity loss of $Li(Li_{0.2}Mn_{0.54}Ni_{0.13}Co_{0.13})O_2$ composited with various MoO_3 contents at 0.1 C between 2.5 and 4.8 V. Reproduced with permission.[70] Copyright 2014, Elsevier. c) Cyclic performances of $Li_{1.2}Mn_{0.56}Ni_{0.12}Co_{0.12}O_2$ prepared by solvothermal or coprecipitation methods at 0.5 C between 2.0 and 4.8 V, inset is the schematic illustrations of the solvothermal and the coprecipitation methods. Reproduced with permission.[71] Copyright 2015, Royal Society of Chemistry. d) Rate performance of pristine and sodium doped $0.5LiNi_{1/3}Co_{1/3}Mn_{1/3}O_2{\cdot}0.5Li_2MnO_3$, and schematic illustration of gradient surface Na^+ doping. Reproduced with permission.[61] Copyright 2016, Wiley-VCH.

voltage fading is restrained. To verify this target, Guo and coworkers compared the electrochemical behaviors of LL-111 ($0.5Li_2MnO_3 \cdot 0.5LiNi_{1/3}Co_{1/3}Mn_{1/3}O_2$) with LL-811 ($0.5Li_2MnO_3 \cdot 0.5LiNi_{0.8}Co_{0.1}Mn_{0.1}O_2$).[133] The LL-811 significantly outperforms the LL-111 in cyclic stability, as its average voltage only decays for 201 mV after 200 cycles, whereas the LL-111 experiences a voltage drop of ≈700 mV only after 100 cycles (Figure 5c).

© 2019 WILEY-VCH Verlag GmbH & Co. KGaA, Weinheim

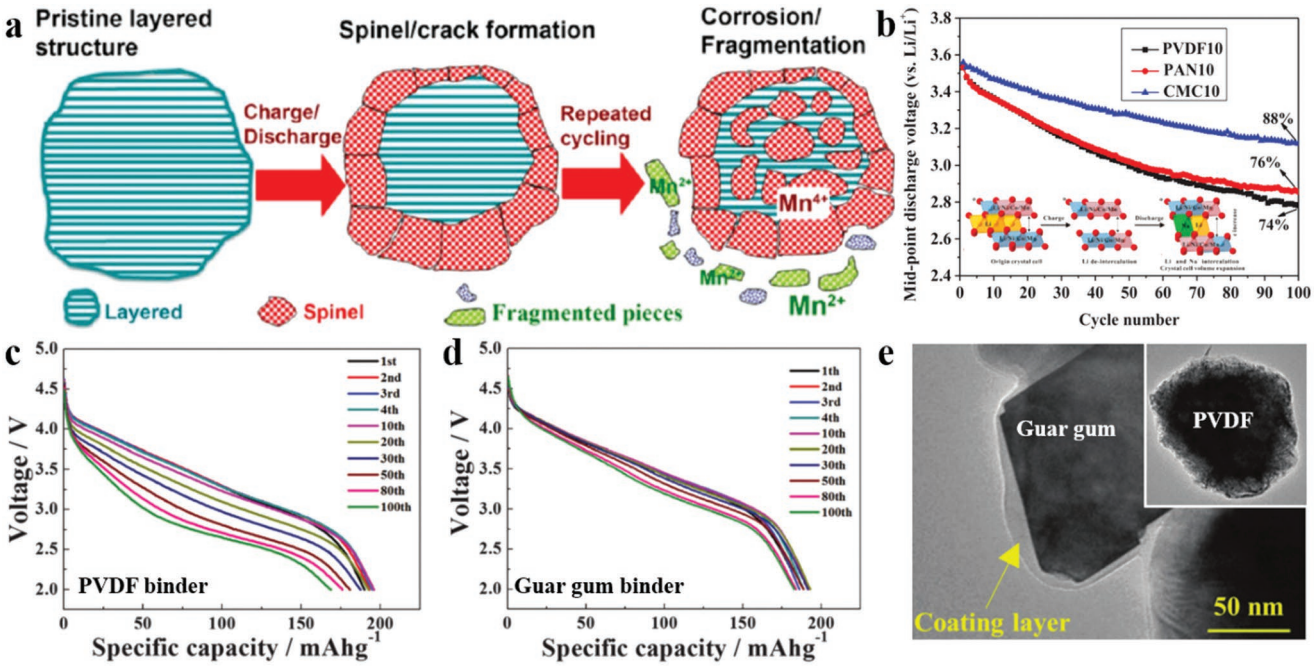

Figure 4. a) Schematic of phase transformation from layered to spinel and the corresponding corrosion process of LL. Reproduced with permission.[116] Copyright 2013, American Chemical Society. b) Midpoint discharge voltage plots at 20 mA g^{-1} of $Li_{1.2}Ni_{0.13}Co_{0.13}Mn_{0.54}O_2$ with polyvinylidene fluoride (PVDF), polyacrylonitrile (PAN), or sodium carboxymethyl cellulose (CMC) as binder and the proposed Li^+/Na^+ ion-exchange mechanism of CMC. Reproduced with permission.[117] Copyright 2017, Wiley-VCH. Discharge curves at 100 mA g^{-1} of $Li_{1.14}Ni_{0.18}Mn_{0.62}O_2$ electrode prepared with c) PVDF or d) guar gum binder. e) Corresponding TEM images of the $Li_{1.14}Ni_{0.18}Mn_{0.62}O_2$ particles after 200 cycles. Reproduced with permission.[118] Copyright 2016, Royal Society of Chemistry.

2.2.3. $R\bar{3}m$–$C2/m$–$Fd\bar{3}m$ (LLS) Category

Extending from the blueprint of incorporating spinel into LL, the $R\bar{3}m$–$C2/m$–$Fd\bar{3}m$ heterostructured cathode (LLS) is currently the most complex and best performing category of the heterostructured material family. Theoretically, these ternary composites have the ideal electrochemical parameters in all aspects, including reversible capacity above 300 mAh g^{-1}, negligible initial capacity loss, superior rate capability, and stable cyclability. The LL in the composite can provide large sources of Li^+ for insertion/extraction owing to presence of Li_2MnO_3. Meanwhile, the $Fd\bar{3}m$ component provides 3D Li^+ diffusion channels and 16*c* octahedral empty sites.[134] The former feature accelerates Li^+ kinetic following the same mechanism as the LS materials, while the latter property affords the capability to accept extra Li^+ in the initial discharge at 3.0 V and narrows the inital charge and discharge capacity gap. XRD, Raman spectroscopy, and polycrystalline selected area electron diffraction (SAED) are commonly applied to confirm the formation of LLS cathodes via direct structural evidences. **Figure 6**a shows an example where structural signals of all three components are found in the XRD pattern. In which, diffraction peaks attributed to $Fd\bar{3}m$ symmetry are clearly observed in addition to peaks associated with the $R\bar{3}m$ symmetry of pristine $LiMO_2$ and the superlattice diffractions of Li_2MnO_3.[135] Raman spectra and SAED can further support the formation of ternary heterostructure with the observation of fingerprint vibration and diffraction of $C2/m$ and $Fd\bar{3}m$ phases (Figure 6b–d).[136,137]

According to the different combination modes between the LL and spinel, the LLS materials can be divided into three categories including mechanical mixing, core–shell, and fully integrated. First, mechanical mixing LL with $Fd\bar{3}m$ spinels is a straightforward method to prepare LLS.[111,138,139] However, samples prepared from this method lack interconnection between the two components, so their overall performance only reflects as average of each phase. Yang and coworkers prepared a series of composite cathodes by mixing $Li[Li_{0.2}Mn_{0.54}Ni_{0.13}Co_{0.13}]O_2$ with $Fd\bar{3}m$ spinel $LiMn_{1.5}Ti_{0.5}O_4$ materials.[138] The as-prepared composite materials exhibit characteristic voltage plateaus of both LL and spinel (Figure 6e), with the plateau length proportional to the ratios of each phase. Upon increasing percentage of the spinel component, the initial coulombic efficiency, cyclic performance, and capacity retention at high rates are improved in spite of reduced specific capacity (Figure 6f–h). Gao and Manthiram also demonstrated a similar tendency through blending LL with spinel $Li_4Mn_5O_{12}$ at different ratios, and proved that it is possible to completely inhibit the initial capacity loss by adding 30 wt% $Li_4Mn_5O_{12}$.[111]

Distribution of crystal phases in the second type of LLS can be described with typical core–shell architecture, which is illustrated in **Figure 7**a. Surface treatment on LL is the most common approach to attain such structure, in which the spinel component is added as coating shells to stabilize the LL core and provide additional pathway for rapid Li^+ diffusion. Based on this idea, Wu et al. designed a heterostructured cathode (SLH) by encapsulating $Li_{1.2}Mn_{0.6}Ni_{0.2}O_2$ with a spinel nanoshell of $LiMn_{2-x}Ni_xO_4$.[135] The core–shell assembly

© 2019 WILEY-VCH Verlag GmbH & Co. KGaA, Weinheim

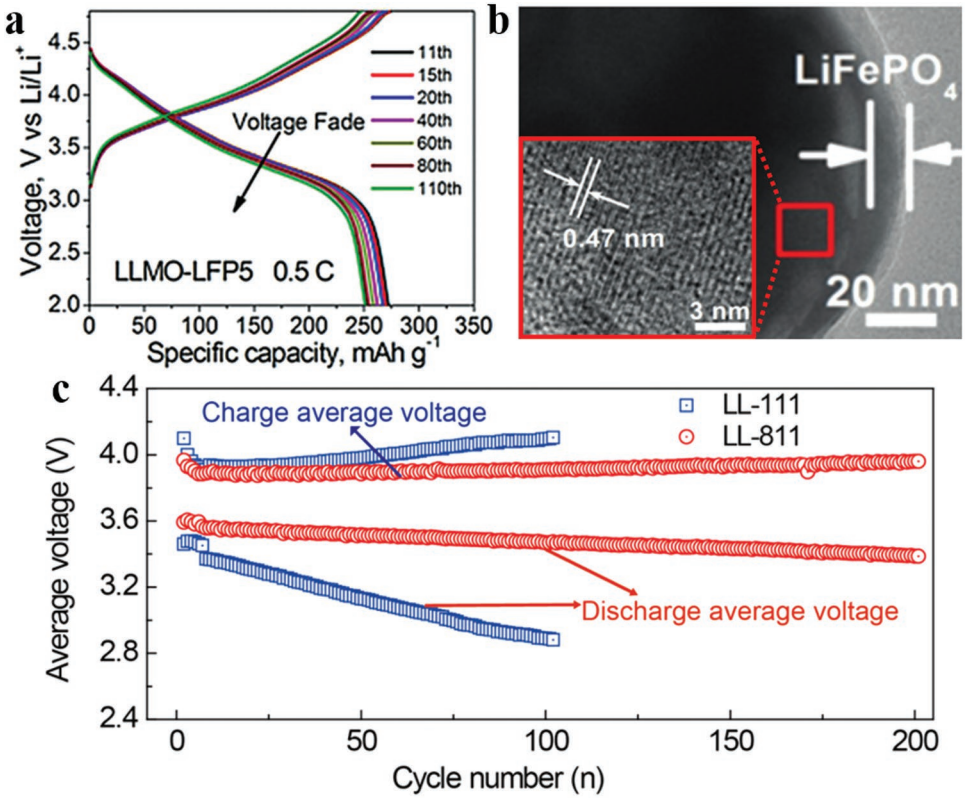

Figure 5. a) Charge and discharge profiles at 0.5 C of 5 wt% $LiFePO_4$ modified $Li_{1.2}Ni_{0.13}Co_{0.13}Mn_{0.54}O_2$ (LLMO-LFP5). b) TEM image of LLMO-LFP5 after 120 cycles of charge and discharge. Reproduced with permission.[126] Copyright 2015, Wiley-VCH. c) Average voltage versus cycle numbers graph of $0.5Li_2MnO_3{\cdot}0.5LiNi_{1/3}Co_{1/3}Mn_{1/3}O_2$ (LL-111) and $0.5Li_2MnO_3{\cdot}0.5LiNi_{0.8}Co_{0.1}Mn_{0.1}O_2$ (LL-811) electrodes. Reproduced with permission.[133] Copyright 2016, American Chemical Society.

is easy to distinguish with an interface between the layered and spinel regions that exhibit two distinctly different sets of lattice orientations (Figure 7b). When the spinel shell is present, an extra voltage plateau representing typical $Fd\bar{3}m$ spinel behavior is observed in the discharge profile of SLH (Figure 7c), which enlarges the 0.1 C discharge capacity from 283.5 to 300.0 mAh g^{-1}. According to the rate capability test, the pristine $Li_{1.2}Mn_{0.6}Ni_{0.2}O_2$ (PL) experiences continuous capacity fading in the first 20 cycles. Conversely, as demonstrated in Figure 7d, SLH yields greatly improved capacities at all cycling rates and negligible capacity lost. Thereafter, a PVP assisted method was also proposed by the same group to fabricate ultrathin spinel membrane-encapsulated LL, which demonstrates superior electrochemical properties compared to untreated LL (Figure 7e–g).[140] AlF_3 coating, carbon coating, and acid treatment were also reported as feasible strategies to induce phase transition of surface LL to spinel and improve material performances.[67,96,98,137,141–144] For example, a layered-to-spinel phase transformation of LL surface was induced by Li^+ leaching after AlF_3 coating, which increases the material initial coulombic efficiency from 82.8% (pristine) to 197.1% (10 wt% AlF_3 coating) at 20 mA g^{-1} and capacity retention at 500 mA g^{-1} (vs capacity at 25 mA g^{-1}) from 68% (pristine) to 76% (1 wt% AlF_3 coating).[98] In another example, a carbonization-reduction method based on polydopamine was introduced to fabricate L@S@carbon heterostructured cathode with a capacity as high as 334.5 mAh g^{-1} at 25 mA g^{-1}, as well as enhanced rate and cyclic performance.[141]

Although surface treatments on LL provide possibility to obtain core–shell LLS with balanced electrochemical performances, their rigorous preparation processes have hindered their feasibility in large-scale productions. This issue can be avoided by exploration of one step processes that rationally modify different synthesis conditions to obtain LLS with integrated $Fd\bar{3}m$ spinel and LL (**Figure 8**a).[136,145–148] In this type of LLS, layered and spinel particles are aggregated to form secondary architecture with adequate distribution and nanoscale interconnection. As an example, the Sun group reported a solvothermal method with controlled heat treatment for one-step preparation of LLS $Li_{1.16}Mn_{0.6}Ni_{0.12}Co_{0.12}O_2$ with scattered $Li_4Mn_5O_{12}$ spinel nanoparticles. Successful synthesis of the material with desired phase distribution was confirmed by high-resolution TEM (HRTEM), fast Fourier transform (FFT), and Mn *k*-edge X-ray absorption near edge structure (XANES) (Figure 8b,c).[136] The calcination temperature of 650 °C was identified to be critical in promoting the formation of spinel components through a "Li-rich spinel phase decomposition" mechanism.[146] As shown in Figure 8d, compared to LL, the presence of $Li_4Mn_5O_{12}$ with tetravalence Mn in LLS leads to a decrease of 27 mAh g^{-1} in charge capacity and increase of 24 mAh g^{-1} in discharge capacity, which raises the initial coulombic efficiency by

© 2019 WILEY-VCH Verlag GmbH & Co. KGaA, Weinheim

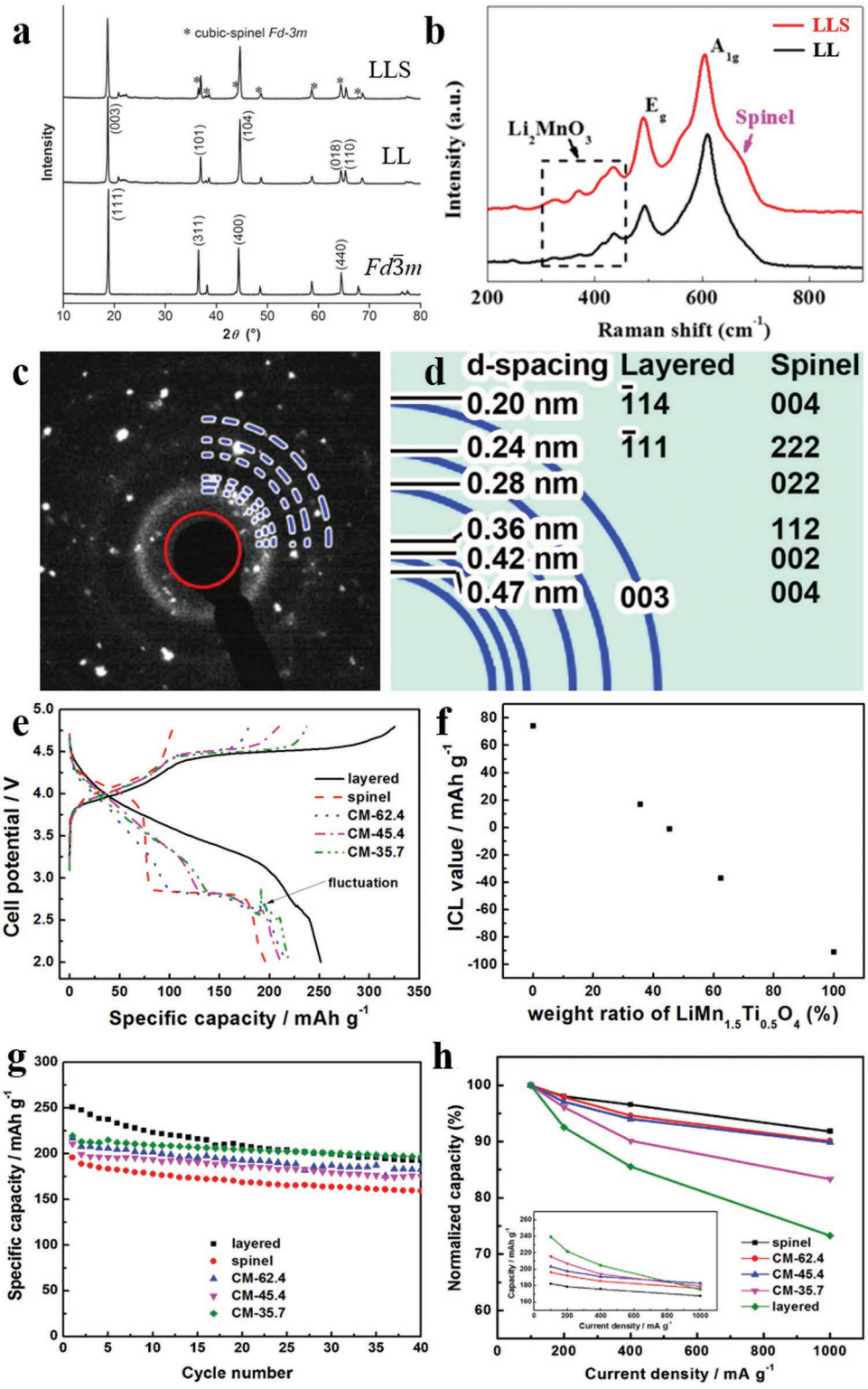

Figure 6. a) XRD patterns of LLS compared against LL and $Fd\bar{3}m$ spinel references. Reproduced with permission.[135] Copyright 2013, Wiley-VCH. b) Raman spectra of LLS and LL. Reproduced with permission.[136] Copyright 2014, American Chemical Society. c) Electron diffraction pattern and d) corresponding index of LLS. Reproduced with permission.[137] Copyright 2013, Springer Nature. e) Initial charge and discharge profiles, f) irreversible capacity loss (ICL) graph, g) cyclic performance, and h) normalized rate performance of composite cathodes with different ratio of $Li_{1.2}Mn_{0.54}Ni_{0.13}Co_{0.13}O_2$ and $LiMn_{1.5}Ti_{0.5}O_4$. The numbers in CM-62.4, CM-45.4, and CM-35.7 represent the weight percent of $LiMn_{1.5}Ti_{0.5}O_4$ in the final composites. Reproduced with permission.[138] Copyright 2014, Elsevier.

© 2019 WILEY-VCH Verlag GmbH & Co. KGaA, Weinheim

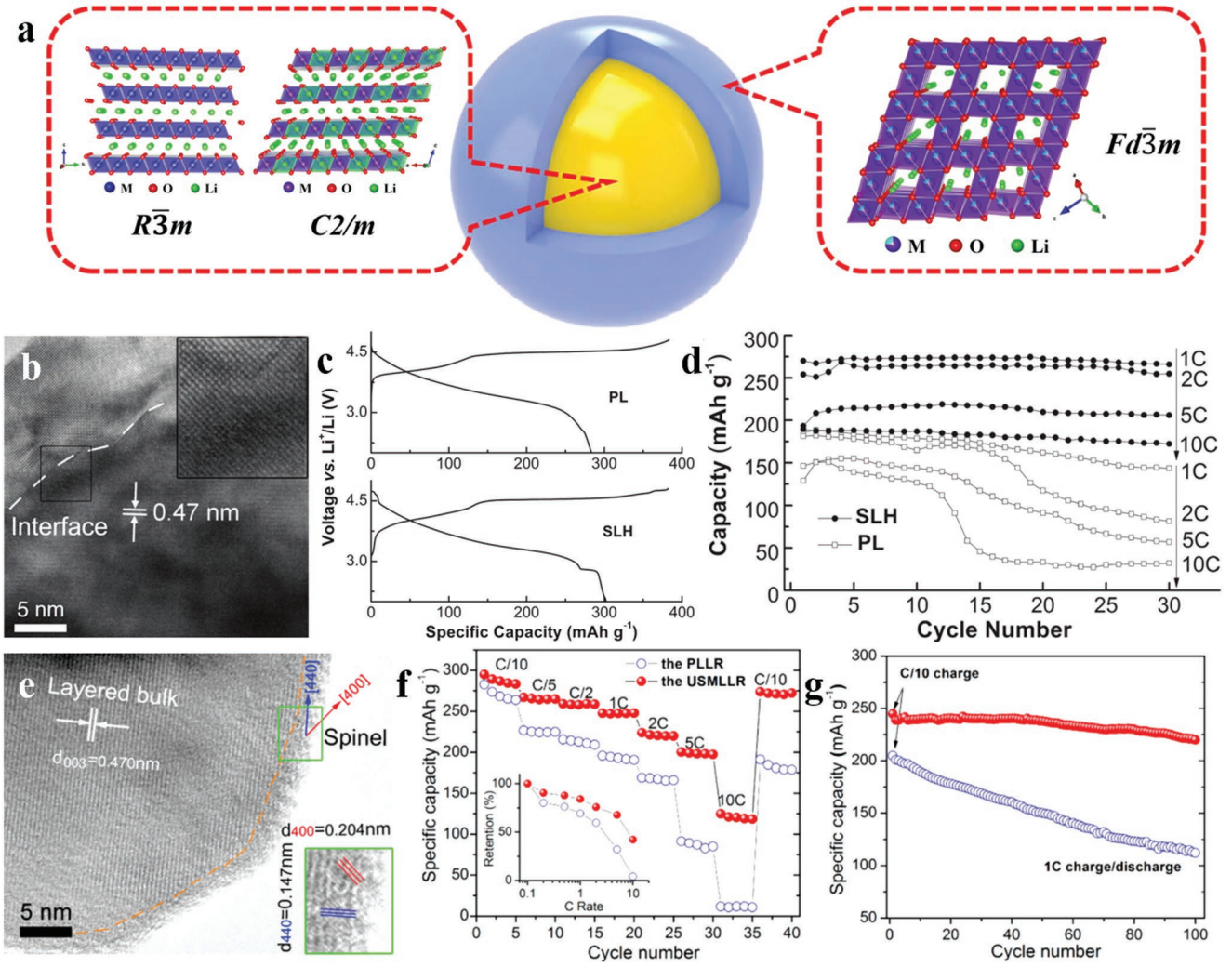

Figure 7. a) Schematic of core–shell type for LLS. Reproduced with permission.[26] Copyright 2018, WILEY-VCH. b) HRTEM image of spinel/layered heterostructured (SLH) particles; c) 0.1 C initial charge and discharge curves; d) capacity retention at various cycling rates of pristine layered (PL) $Li_{1.2}Mn_{0.6}Ni_{0.2}O_2$ and SLH. Reproduced with permission.[135] Copyright 2013, Wiley-VCH. e) HRTEM image of ultrathin spinel membrane encapsulated-layered Li-rich cathode (USMLLR), inset is the enlarged view of the area surrounded by the green rectangle; f) rate capabilities and g) 1 C cyclic performance of USMLLR and pristine layered Li–rich materials (PLLR). Reproduced with permission.[140] Copyright 2014, American Chemical Society.

about 14%.[136] The rate capability of the materials is also elevated significantly by 138 mAh g^{-1} at the cycling rate of 10 C (Figure 8e). Another study systematically evaluated the influence of total calcination time, and used the result to further optimize the preparation conditions for integrated type LLS.[134] Figure 8f compares XRD patterns of LLS prepared with 24 h (T24) and 36 h (T36) of 650 °C calcination. The negative peak shift of T24 indicates its larger cubic lattice parameters, and thus widened 3D channels for Li^+ diffusion (Figure 8h); its spinel content is also higher than T36 based on Rietveld refinement results. When the treatment time is further lowered to 12 h (T12), a poorly ordered crystal structure is formed with the highest Li^+/Ni^{2+} cation mixing and lowest spinel contents. The electrochemical measurements confirm the superiority of T24 with a coulombic efficiency of 101% at a rate of 0.2 C and a high capacity of 206 mAh g^{-1} at 10 C (Figure 8g,i). Some of these electrochemical parameters reported in 2016 remain to be top tiers among cathode candidates of LIBs published in scientific journals.

3. SIBs

3.1. Single-Phase Cathode

3.1.1. Layered Structure

Similar to $LiMO_2$, layered Na_xMO_2 commonly used as cathodes in SIBs are also built up by alternate layers of edge-sharing octahedral MO_6 and adjacent Na^+. The sodium coordination in these crystal phases can exist in several polytypes with different oxygen layers stacking, which generates different intercalation sites for Na^+. To distinguish the structural properties of cathodes for SIBs, researchers have set naming rules according to

© 2019 WILEY-VCH Verlag GmbH & Co. KGaA, Weinheim

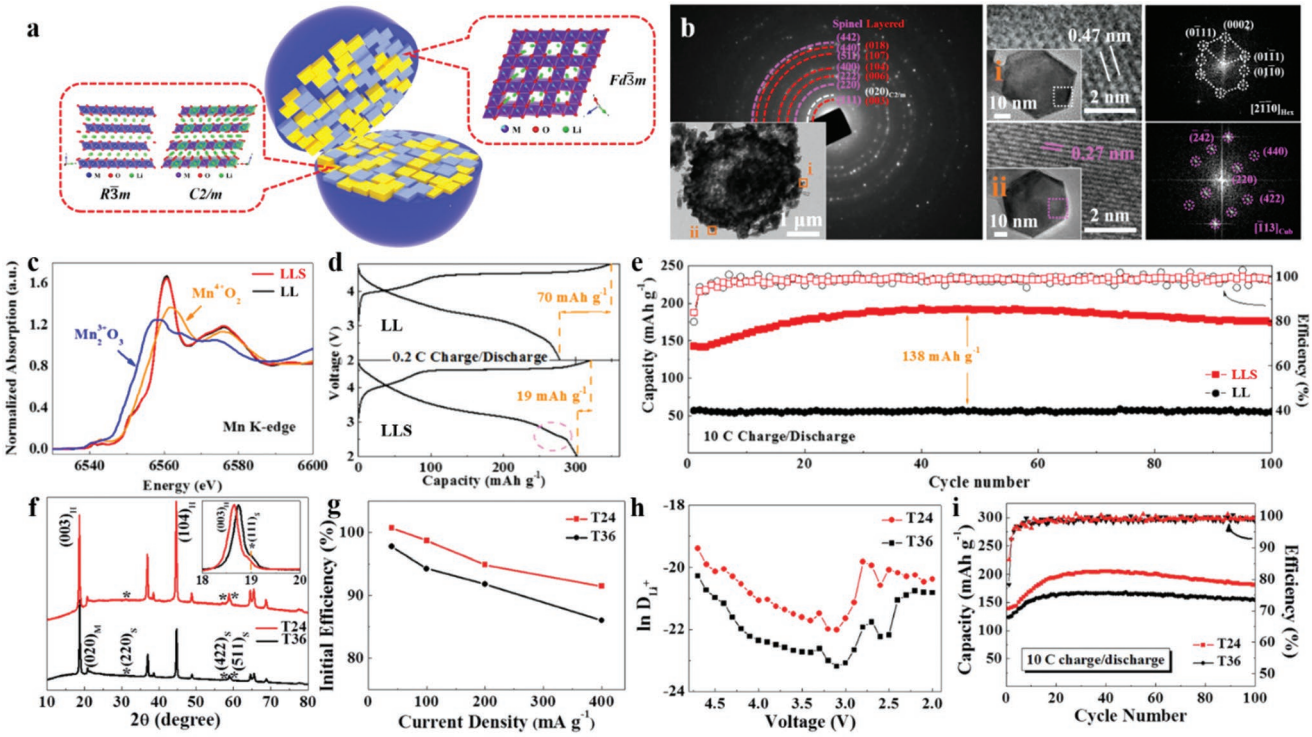

Figure 8. a) Schematic illustration of the integrated type for LLS. Reproduced with permission.[26] Copyright 2018, Wiley-VCH. b) TEM image, SAED patterns, HRTEM images, and FFT patterns of LLS. c) Mn *k*-edge XANES spectra, d) initial charge and discharge curves, e) 10 C cyclic performance (2 A g^{-1}) between 2.0 and 4.8 V of LL and LLS. Reproduced with permission.[136] Copyright 2014, American Chemical Society. f) XRD patterns, g) initial efficiencies at different current density, h) ln D_{Li^+} (D_{Li^+} represents Li^+ chemical diffusion coefficient, cm^2 s^{-1}) plots at the first discharge and i) cyclic performance at 10 C (2 A g^{-1}) between 2.0 and 4.8 V of $Li_{1.140}Mn_{0.622}Ni_{0.114}Co_{0.124}O_2$ obtained via 24 h (T24) or 36 h (T36) calcination at 650 °C. Reproduced with permission.[134] Copyright 2016, Royal Society of Chemistry.

the stacking arrangement of M layers and Na^+ accommodated sites. O3 and P2 are the two main types of layered oxides and they exhibit different electrochemical properties. As demonstrated in **Figure 9**, the letter O/P reflects the octahedral and trigonal prismatic coordination of Na^+, respectively; the numeral following the letter indicates the number of transition metal layer per unit cell.[149–151]

Stable O3-layered Na_xMO_2 commonly have x value close to 1 and M ions with average oxidation state of ≈3. Their framework can be assigned to cubic close-packed (ccp) oxygen array. The Na^+ and 3d M ions accommodate distinct octahedral sites due to their different ionic radius (Na^+ is 1.02 Å and M is less than 0.7 Å). While the Na and M layers are formed via edge-sharing NaO_6 and MO_6 octahedral subunits ordered into alternate layers perpendicular to.[111] The M layers can adapt three different types of O stacking, which include the AB, CA, and BC crystallographic configurations. The letters A, B, and C represent different sites in the MO_2 layers with distinguish oxygen atom arrangement as marked in Figure 9. The O3-layered structure can also be regarded as cation-ordered rock salt superstructure oxides, or as $R\bar{3}m$ phase materials. A prime symbol is usually added to represent the in-plane distortion in the crystal lattice, such as the one in O′3-$NaNiO_2$ used to indicate a $C2/m$ monoclinic lattice.[152] When provided with sufficient Na^+ during cycling, O3-cathodes usually show reversible capacity exceeding 150 mAh g^{-1} with high initial coulombic efficiency, and they generally have higher capacity in the same voltage window than their polytype of P2-Na_xMO_2.[153,154] However, upon charging, the originally occupied edge-sharing MO_6 octahedral sites would slowly change to prismatic sites, which transforms the material from O3 to P3 phase and generates Na^+ vacancies. Such phase transformation leads to voltage fading in most Na_xMO_2 and reduces the energy density with nearly half of the capacity lost.[155] Study by Komaba et al. on $Na_{1-x}Ni_{0.5}Mn_{0.5}O_2$ suggests that the O3-$NaNi_{0.5}Mn_{0.5}O_2$ undergoes a phase transformation from O3, O′3, P3, P′3 to P3″ during the Na^+ extraction process (**Figure 10**a,b) in the voltage window of 2.0–4.5 V (vs Na/Na^+).[156] When most of the sodium is extracted by charging the batteries to 4.5 V, the P3″ phase with highly faulted layered structure can be found. This complex phase transition severely limits cyclic stability of cathodes.

As for P2-Na_xMO_2, they are categorized by crystal structures constructed with two types of MO_2 layers (AB and BA layers) with Na^+ occupying two trigonal prismatic sites: Na_f on the facet and Na_e at the edge. The Na_f sites contact the two octahedral MO_6 of the adjacent slabs along its facets, while the Na_e sites link with six surrounding octahedral MO_2 along its edges. These adjacent Na_f and Na_e sites cannot be simultaneously occupied due to the large coulombic repulsion between two adjacent Na^+. As such, Na^+ would be evenly distributed to the 2D triangle (prismatic) lattices, which minimizes the in-plane repulsive interaction. P2-layered structure is classified with 2H phase (space group: $P6_3/mmc$). Although this structure usually has low initial Na content in a half-cell setting as

© 2019 WILEY-VCH Verlag GmbH & Co. KGaA, Weinheim

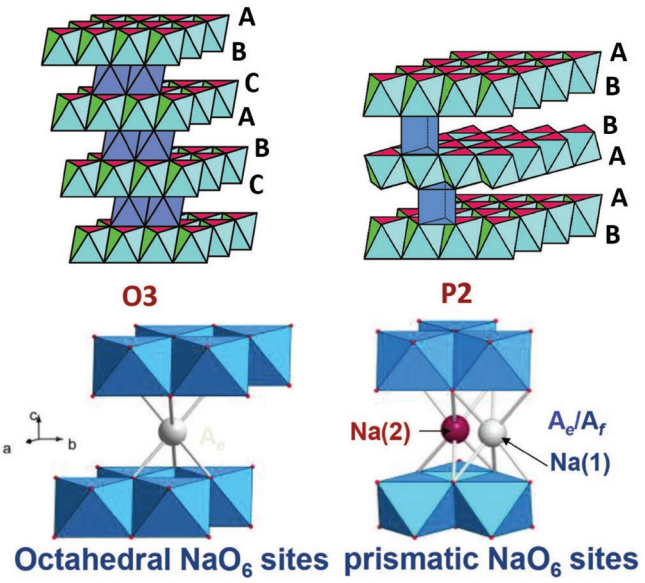

Figure 9. Structural illustration of O3 and P2-$NaMO_2$ layered oxides. The sodium intercalation site is also presented for the two crystal structures. Reproduced with permission.[150] Copyright 2018, Wiley-VCH.

shown by studies of Komaba and co-workers and Delmas and co-workers, the P2 phase possesses larger reversible capacity than O3-$Na_xFe_yMn_{1-y}O_2$.[157,159] As shown in Figure 10c, the O3-$NaFe_{1/2}Mn_{1/2}O_2$ delivers 100–110 mAh g^{-1} between 1.5 and 4.2 V, which is obviously inferior to the P2 counterpart with capacity above 190 mAh g^{-1}. Nevertheless, the limited Na content in the pristine P2-materials causes them to have lower initial charge capacity than the corresponding discharge capacity (Figure 10d), and results in unsatisfactory coulombic efficiency in full cell.[158] During desodiation, the crystal phase of the material transforms from P2 to O2, and vice versa during sodiation. The P2 to O2 transformation process is electrostatically favored and can be explained by Na^+ vacancies being less stable in prismatic sites than in octahedral sites; the screening of repulsive O^{2-}–O^{2-} interactions by Na^+ is also less effective with lesser Na^+ residue in the interslab space.[160] With stronger M—O bonds and simpler phase transformation, the P2-structure usually possesses superior cyclic stability compared to the O3. A lower diffusion barrier is also expected in the P2-phase due to its wider diffusion path for Na^+. The Na^+ migrates from prismatic sites to its adjacent sites via open square bottlenecks that are surrounded by four oxygen ions, which enforce weaker repulsion compared to the interstitial tetrahedral sites in O3-structure, and thus generally lead to better rate performance.[161,162]

3.1.2. Tunnel Structure

Another sodium deficient phase in the Na—Mn—O family is tunnel structured $Na_{0.44}MnO_2$, which is isostructural to $Na_4Mn_4Ti_5O_{18}$ and first reported by Mumme in 1968.[163] The framework of $Na_{0.44}MnO_2$ (space group: *Pbam*) is constructed by four octahedral MnO_6 sites and one octahedral MnO_5 site (**Figure 11**a).[164] These square pyramidal and octahedral sites are linked to each other by either edge or vertex/corner sharing. Each of the MnO_5 site serves as linkage for one triple octahedral chain and two double octahedral chains, establishing two types of tunnels that relief lattice strains during insertion/extraction of Na^+, which results in excellent cyclic performance. The special crystal orientation also leads to the formation of three different Na sites in tunnel $Na_{0.44}MnO_2$, including the Na1, Na2, and Na3 sites; the Na2 sites can be further divided into two sites in distinct environments (Na21 and Na22, Figure 11b). The Na1 sites in the small tunnel are almost entirely filled all time, whereas the other sites (Na2 and Na3) in the S-shaped tunnels are approximately half filled, which benefits Na^+ diffusion and rate performance. During discharge (reduction), Na^+ inserts into tunnels and causes the materials to undergo a biphasic evolution to the structurally similar $Na_{0.67}MnO_2$ that delivers a capacity of 120 mAh g^{-1}. Multiple crystal structures with different sodium configurations and compositions may form during this process, but they are in similar energy thermodynamically. As a result, the material would exist as a mixture of various local configurations with similar stability without long-range ordering, which is beneficial for battery lifetime. Nevertheless, the intrinsically low reversible capacity of the materials remains to be a major challenge for application of the material in SIBs (Figure 11c,d).[165]

3.2. Developing Layer-Based Heterostructured Cathode for SIBs

In the past decades, inspiring strategies have been proposed and extensively investigated to promote performance improvement of single-phase SIB cathodes. They can be categorized into morphology design, heteroatom doping, and surface coating. In the category of morphology constructions, such as microsheets,[166] nanosheet aggregated microspheres[167,168] and spherical aggregation of radially aligned hierarchical columnar[169] have been explored to optimize mechanical properties, tap-density, conductivity, and electrode/electrolyte interface. For example, Sun and co-workers successfully prepared sphere-like aggregations with radially aligned hierarchical columnar that have an interior of $NaNi_{0.75}Co_{0.02}Mn_{0.23}O_2$ and an exterior of $NaNi_{0.58}Co_{0.06}Mn_{0.36}O_2$.[169] This cathode material simultaneously realizes efficient utilization of the high capacity nickel-rich core and high stability, which allow it to perform a capacity of 157 mAh g^{-1} and retain 80% of the capacity after 300 cycles. Performance modifications through compositional modification by metal ions including Mg^{2+},[170] Zn^{2+},[171] Cu^{2+},[172,173] and Ti^{4+}[174] were also reported. For instance, Bruce and co-workers performed systematic investigations on the influence of Mg substitution in $Na_{2/3}Mg_{0.28}Mn_{0.72}O_2$.[175,176] It was discovered that the change provides smoother electrochemistry, increases rate performance and capacity retention, which can be explain by the reduced amount of Mn^{3+}, delayed phase transformation, and lattice oxygen stabilization by Mg^{2+} at high voltage . Finally, to address the atmospheric and electrochemical corrosion on layered cathodes, surface coating layers including spinel-like titanium (III) oxides, β-$NaCaPO_4$, Al_2O_3, etc., were designed to scavenge HF and H_2O, which would stabilize electrode/electrolyte interface and promote ion diffusion.[177–180]

Although encouraging experimental results were reported, increments offered by these strategies are relatively small, while

© 2019 WILEY-VCH Verlag GmbH & Co. KGaA, Weinheim

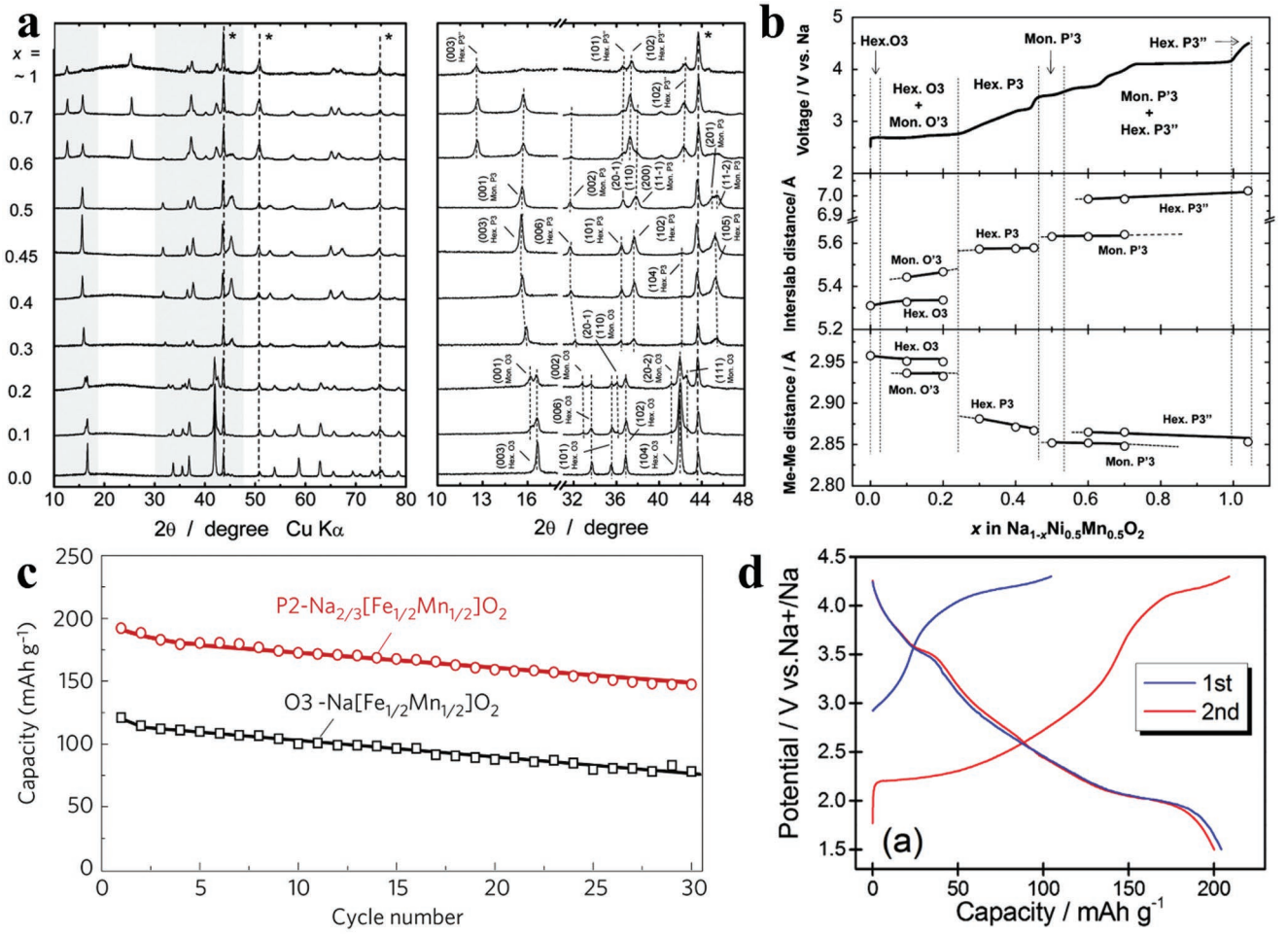

Figure 10. a) Complete (left) and expanded (right) ex situ XRD patterns of the $Na_{1-x}Ni_{0.5}Mn_{0.5}O_2$; b) phase evolution and changes in crystallographic parameters of $Na_{1-x}Ni_{0.5}Mn_{0.5}O_2$ with Na^+ content. Reproduced with permission.[156] Copyright 2012, American Chemical Society. c) Discharge capacity profiles of P2 and O3-$NaFe_{1/2}Mn_{1/2}O_2$.[157] Copyright 2012, Springer Nature. d) Charge and discharge curves at the initial two cycles of P2-$Na_{0.67}Fe_{0.35}Mn_{0.65}O_2$. Reproduced with permission.[158] Copyright 2014, Elsevier.

marginal performance leaps are needed to meet the requirements of standard applications. A possible path of achieving such status is through exploration of heterostructured composites that integrate advantages of different crystal phases while overcoming their intrinsic defectiveness. Compatibility in physical and chemical properties, preparation processes, and crystal structures are the main criteria for composite structure design.[181] Therefore, the investigations of heterostructured cathode have mainly focused on P2–O3 and P2–tunnel heterostructured cathodes, but other types of heterostructured cathodes like P3–P2, P2–O2 are also reported with encouraging results.

3.2.1. Layered–Layered Category

P2–O3 Type: As described above, pure O3 and P2 layered materials each have their intrinsic advantages and disadvantages. In 2014, Johnson and co-workers introduced small amount of Li^+ into O3-$NaNi_{0.5}Mn_{0.5}O_2$.[182] Interestingly, it was discovered that some of the Li^+ reside in the octahedral sites of the Na layers and induce unique intergrowth of P2–O3 phased materials at the atomic scale (**Figure 12**a–d). The Na–P2 phase and Li–O3 phase would grow following the increase of Li content. This unique P2–O3 composite shows superior specific capacity and rate capability to that of pure O3-cathodes. In situ synchrotron XRD (SXRD) investigations (Figure 12e) of the composite between 2.0 and 4.05 V reveal that the P3-phase in the P2–P3 intergrowth structure did not suffer the Na^+ diffusion energy penalty observed in the transition between the P3 and O3 phases. This allows the P-phase to take full advantages of the fast Na^+ diffusion between the trigonal prismatic sites, which brings improved rate performance. Nevertheless, the O3-phase would still undertake the O3–P3 phase transformation during cycling that limits the cycle life to 20 cycles with capacity of 140 mAh g^{-1}. With the aim to further promote the development of P2–O3 composite cathodes, Zhou and co-workers integrated minor amount of O3 (5.78 wt%) into a P2 cathode (94.22 wt%) and obtained the composite $Na_{0.66}Li_{0.18}Mn_{0.71}Ni_{0.21}Co_{0.08}O_{2+d}$ (Figure 12f,g).[183] This was implemented by coprecipitation and subsequent solid-state reaction of Li-containing compounds. The resulting P2–O3 composite shows the highest energy

© 2019 WILEY-VCH Verlag GmbH & Co. KGaA, Weinheim

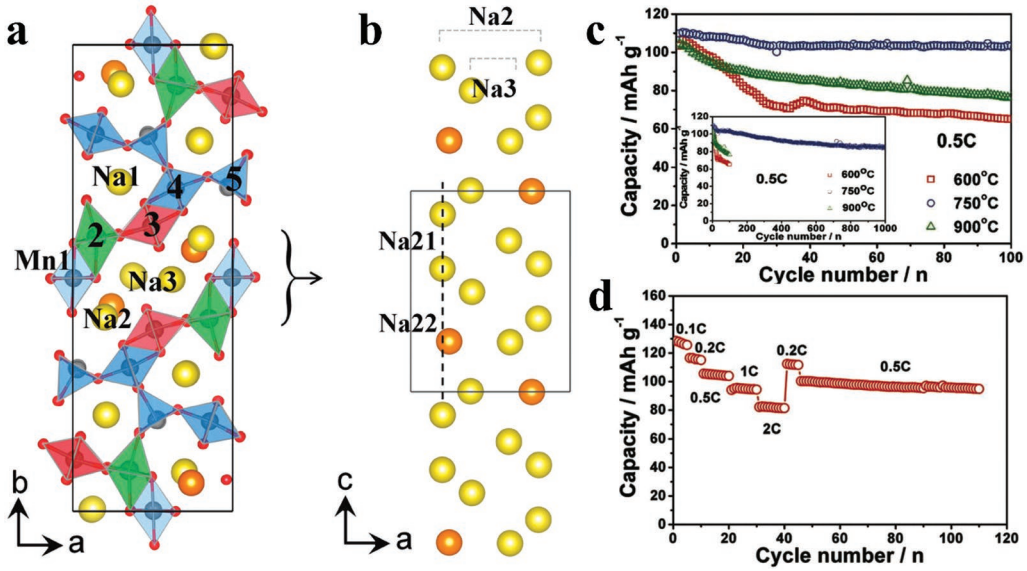

Figure 11. a) Crystal structure illustration of $Na_{0.44}MnO_2$ with three sites for sodium ions and five crystallographic sites for manganese; b) diagram demonstrating the sodium configuration in $Na_{0.44}MnO_2$, the most probable Na^+ intercalation is in the S-shaped tunnel along the *c*-axis, where the Na2 sites may adapt two different sodium positions (Na21 and Na22). Reproduced with permission.[164] Copyright 2012, American Chemical Society. c) Cyclic performance at 0.5 C (60 mA g^{-1}) of $Na_4Mn_9O_{18}$ samples sintered at 600, 750, and 900 °C. d) Rate performance at 12, 24, 60, 120, and 240 mA g^{-1} of $Na_4Mn_9O_{18}$ nanowires obtained by 750 °C calcination. Reproduced with permission.[165] Copyright 2011, Wiley-VCH.

density of 640 Wh kg^{-1} in a voltage window of 1.5 and 4.5 V with good performance retention after 150 cycles (Figure 12h). The intergrowth interfaces and local crystal structure of the separated O3 and P2 phases were evidenced via SAED, scanning transmission electron microscopy (STEM), annular bright field (ABF), and high-angle annular dark field (HAADF) as demonstrated in Figure 12g.

Follow up efforts to modify the P2–O3 composite cathode were conducted by Li et al., who prepared a P2–O3 composite ($Na_{0.67}Mn_{0.55}Ni_{0.25}Ti_{0.2-x}Li_xO_2$) with minor O3 phase by substituting Ti^{4+} and Li^+ through a facile sol–gel method (**Figure 13**a).[184] The electrochemical results indicated that its overall performance was significantly enhanced because of the additional Li content and O3-phase. Specifically, as shown in Figure 13b,c, $Na_{0.67}Mn_{0.55}Ni_{0.25}Li_{0.2}O_2$ delivers a higher capacity of 158 mAh g^{-1} at 12 mA g^{-1} and an improved operating voltage of 3.1 V in comparison to the Li-free cathode (147 mAh g^{-1} and 2.6 V). The rate capacity is also increased, as the capacity at 1200 mA g^{-1} is raised from 15 to 65 mAh g^{-1}. A step further, Qi et al. reported a series of P2–O3 $Na_xNi_{0.2}Fe_{x-0.4}Mn_{1.2-x}O_2$ composites, and tuned the Fe/Mn ratio to balance the P2–O3 composition for optimal capacity, cyclic stability, and rate capability.[185] In situ XRD analyses of the initial charge and discharge confirm reversible phase transformation of O3–P3–O3′ between 2.5 and 4.0 V (Figure 13d). The optimal $Na_{0.78}Ni_{0.2}Fe_{0.38}Mn_{0.42}O_2$ delivers a capacity of 86 mAh g^{-1} with excellent cyclic and rate performance (Figure 13e,f). However, when the charging cutoff voltage is increased to 4.3 V, the balance between the phases would be broken as the P2 structure suffers damage and the P3 generated from O3 vanishes. With the aim to classify the relationship between crystal structures and electrochemical performance, Xu et al. carried out a comprehensive study from the interfacial microstrain perspective.[186] The resulting P2–O3–O1 heterostructured $Na_xNi_{1/3}Co_{1/3}Mn_{1/3}O_2$ displayed a reversible capacity of 142.8 mA h g^{-1} and a capacity retention of 93% at 15 mA g^{-1} by the 50th cycle, which outperforms the binary phased P2–O3 $Na_xNi_{1/3}Co_{1/3}Mn_{1/3}O_2$ and single-phase P2 $Na_xNi_{1/3}Co_{1/3}Mn_{1/3}O_2$. In operando XRD results demonstrate that the intergrowth region in the composite cathode reliefs interfacial microstrain during high voltage charging and thus improves structure stability.

According to previous reports, the high structural compatibility of P2 and O3 allows for the facile preparation of intergrown P2–O3 composite. The component ratio can be altered by changing the Na^+ content and substituting Li^+ into the structures. However, unlike the solid solution observed with Li-rich oxides, the P2 and O3 phases in the P2–O3 composite usually coexist in the form of mixed single crystal phase nanodomains. The modified performance can mainly be attributed to the suppression of undesired phase transformation and boosted ion diffusion. Also, P3 phase transformed from O3 phase in the composite can be maintained during charge and discharge, which allows better phase evolution and Na^+ diffusion. While the irreversible P2–O2 phase transformation is effectively inhibited to maintain the original structure.

P2–P3 Type: Apart from phase transformation of O3 to P3 and electrochemical desodiation, pure P3 phase can also be prepared by low temperature reactions. The P3 phase has two prismatic sites that are crystallographically identical and generally contains higher sodium content than the P2-phase, which can raise the initial coulombic efficiency. These electrochemical advantages of P2–P3 composite have recently attracted research interest. Chagas et al. first investigated the Na^+ storage properties of P2–P3 $Na_{0.45}Ni_{0.22}Co_{0.11}Mn_{0.66}O_2$ in ionic liquid-based electrolytes (10 mol% NaTFSI in PYR14FSI electrolyte, **Figure 14**a–c).[187] The composite demonstrates a reversible

© 2019 WILEY-VCH Verlag GmbH & Co. KGaA, Weinheim

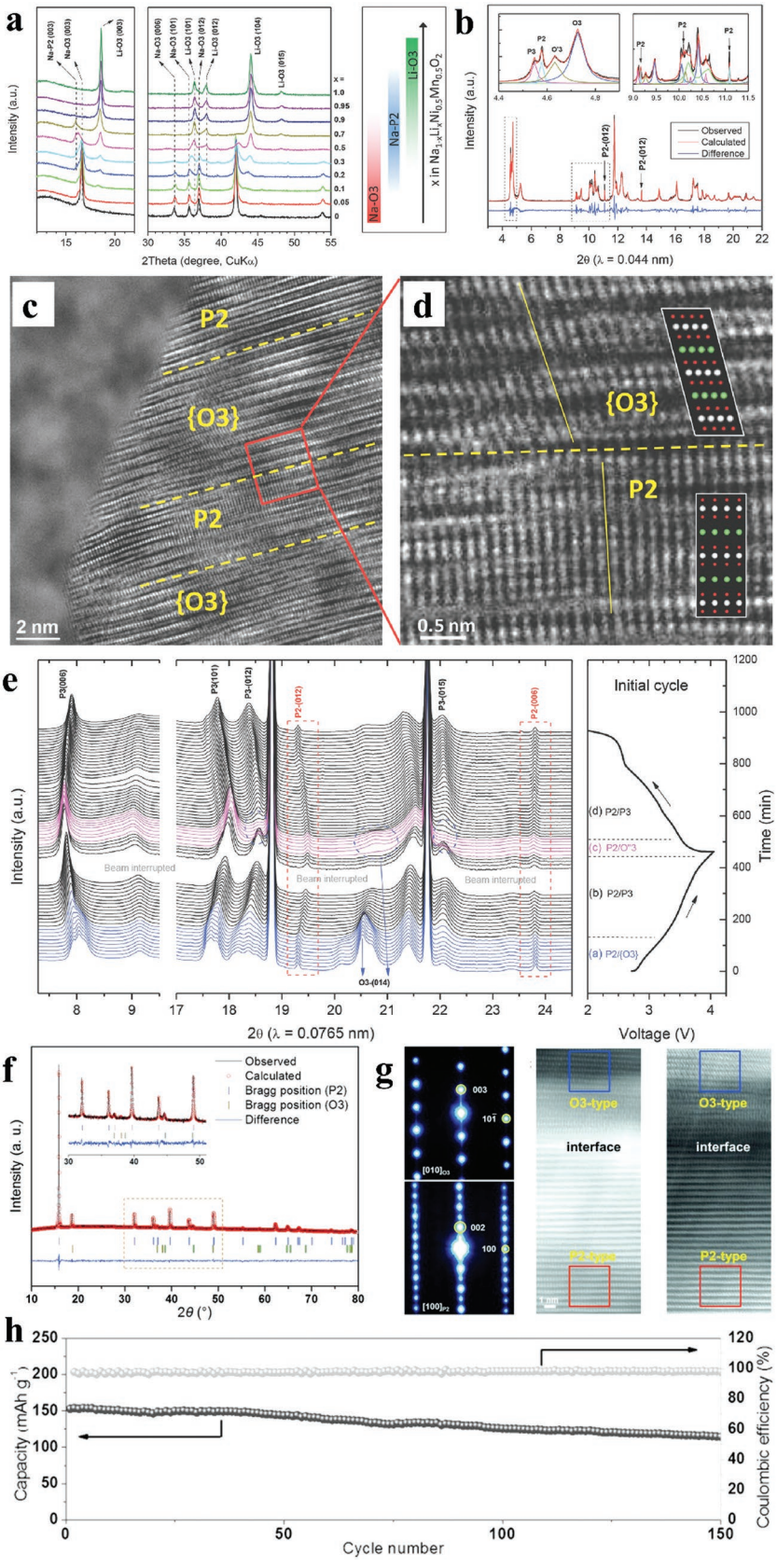

capacity of 200 mAh g^{-1}, a mean voltage at 2.7 V, and capacity retention of 80% after 100 cycles.[188] Systematic research about the effects of synthetic temperature on material performance and crystal structure discovers that varying anneal temperature induces morphology and structure evolution: P3 at 700 °C, P2–P3 at 750 °C, and P2 at 800 or 900 °C.[187] The P2–P3 $Na_xNi_{0.22}Co_{0.11}Mn_{0.66}O_2$ shows a slight voltage increase compared to the P3 counterpart. However, both products reveal fast capacity fading compared to that of the P2-cathode, which can be ascribed to the low crystallinity and smaller particle size. Zhou and co-workers further synthesized biphasic P2–P3 $Na_{0.66}Co_{0.5}Mn_{0.5}O_2$ via a conventional sol–gel route. The P2–P3 composite shows significant improvement in rate capability and cyclic stability, which mainly arise from stable structure and reduced electron transfer resistance.[189]

Multiple Phases: Composite cathodes with more than two phases have also been explored to further optimize electrochemical performance. In a particular study, Keller et al. synthesized P3/P2/O3 layered tertiary composite ($Na_{0.76}Mn_{0.5}Ni_{0.3}Fe_{0.1}Mg_{0.1}O_2$), which integrated Mg^{2+} doping and replaced Co^{3+} with Fe^{3+} (Figure 14d).[190] The composite samples were prepared through solid state reaction based on equilibrium chemistry that varied the sodium content, Mn^{4+}/Ni^{2+} ratio, and synthesis conditions. As a result of the targeted optimization, this triphase composite shows an outstanding capacity of 155 mAh g^{-1} at 18 mA g^{-1} and an energy density of 489.7 Wh kg^{-1} between 2.0 and 4.3 V (Figure 14e), which is superior to the single-phase P2 or O3-cathode. Furthermore, in a narrow voltage range of 2.5–4.3 V, an average discharge potential

Figure 12. a) XRD patterns of $Na_{1-x}Li_xNi_{0.5}Mn_{0.5}O_{2+d}$ ($0 \le x \le 1$). b) High resolution SXRD pattern decomposed into four Na-based phases (O3, O′3, P3, and P2) and one Li-based phase (O3) of $Na_{0.7}Li_{0.3}Ni_{0.5}Mn_{0.5}O_{2+d}$. c,d) HRTEM images which show the intergrowth stacking of P2 and O3 lattices. e) In situ SXRD patterns of $Na_{0.7}Li_{0.3}Ni_{0.5}Mn_{0.5}O_2$ during initial charge–discharge. Reproduced with permission.[182] Copyright 2014, Wiley-VCH. f) XRD patterns and Rietveld refinement of P2–O3 $Na_{0.66}Li_{0.18}Mn_{0.71}Ni_{0.21}Co_{0.08}O_{2+d}$ (NaLiMNC) composite, the inset shows the enlarged diffraction area between 30° and 50°. g) SAED patterns, HAADF STEM, and ABF STEM of the P2–O3 NaLiMNC composite. h) Cyclic performance at 0.5 C of P2–O3 NaLiMNC composite. Reproduced with permission.[183] Copyright 2015, Wiley-VCH.

© 2019 WILEY-VCH Verlag GmbH & Co. KGaA, Weinheim

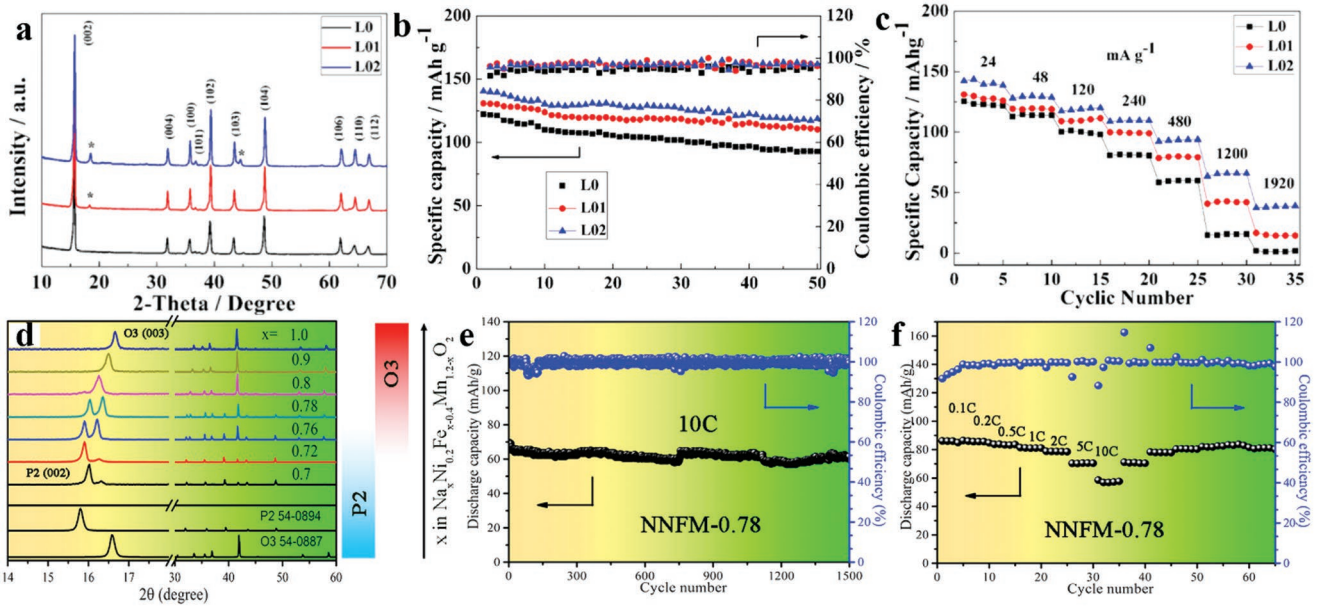

Figure 13. a) XRD patterns, b) cyclic performances at 24 mA g^{-1}, and c) rate performances of $Na_{0.67}Mn_{0.55}Ni_{0.25}Ti_{0.2-x}Li_xO_2$ with $x = 0$ (L0), 0.1 (Li01), and 0.2 (L02). Reproduced with permission.[184] Copyright 2016, American Chemical Society. d) XRD patterns and corresponding crystal phases of $Na_xNi_{0.2}Fe_{x-0.4}Mn_{1.2-x}O_2$ (NNFM) with various Na contents (0.7–1.0) and the resulting phase evolution; e) cyclic stability and f) rate capability of $Na_{0.78}Ni_{0.2}Fe_{0.38}Mn_{0.42}O_2$ (NNFM–0.78). Reproduced with permission.[185] Copyright 2017, American Chemical Society.

of 3.4 V and extraordinary long lifespan of 601 cycles are obtained. It should be noted that the mass ratio of the P-phase is about 41%, which allows the composite to partially inherit the low ion migration barrier of P-phase and achieves significantly improved rate performance (Figure 14f). Finally, the P3/P2/O3 composite also displays satisfying initial coulombic efficiency, which makes the cathode suitable for full-cell match.

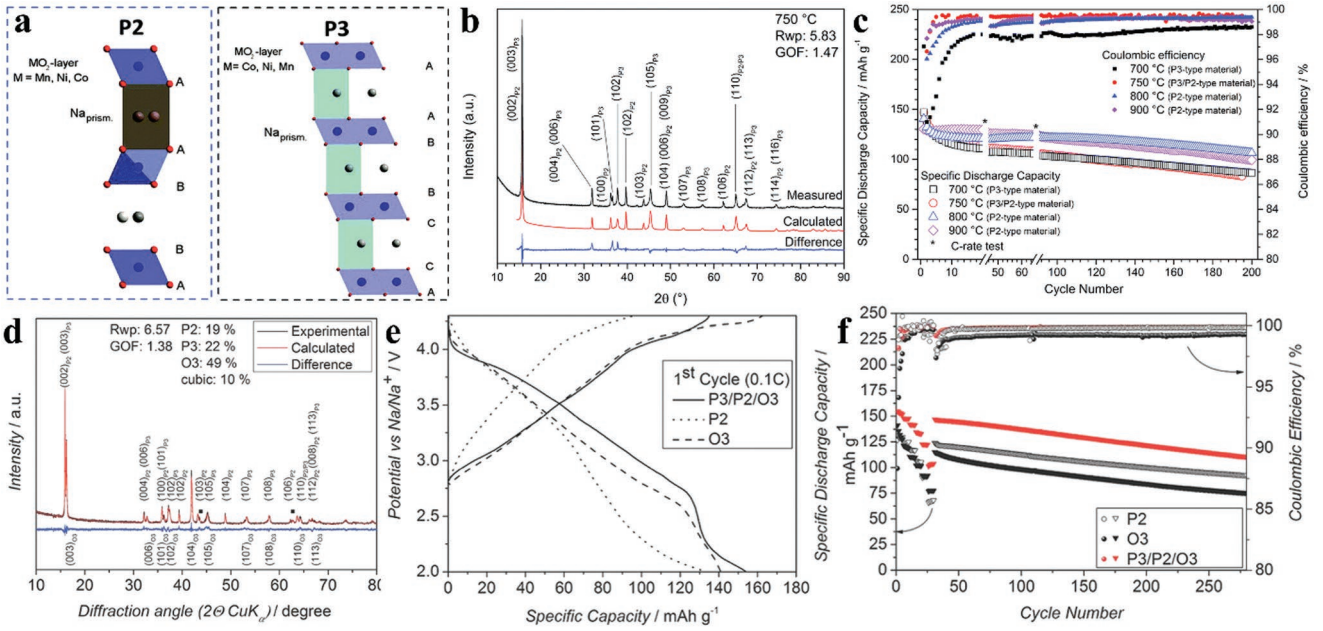

Figure 14. a) Schematic of P2 and P3-$Na_xNi_{0.22}Co_{0.11}Mn_{0.66}O_2$. b) XRD pattern and Rietveld refinement of $Na_xNi_{0.22}Co_{0.11}Mn_{0.66}O_2$ annealed at 750 °C for 6 h. c) Cyclic performance of $Na_xNi_{0.22}Co_{0.11}Mn_{0.66}O_2$ annealed at 700, 750, 800, and 900 °C. Reproduced with permission.[187] Copyright 2014, Royal Society of Chemistry. d) XRD pattern and Rietveld refinement of P3/P2/O3 material with cubic $Mg_{1-x}Ni_xO$ ($x = 0.3$) phase marked by squares. e) Initial charge and discharge curves at 0.1 C (1 C = 180 mA g^{-1}), f) rate performance (0.1, 0.2, 0.5, 1, 2, 5 C) and subsequent 0.2 C cyclic performance of P2-$Na_{2/3}Mn_{0.7}Ni_{0.1}Fe_{0.1}Mg_{0.1}O_2$, O3-$NaMn_{0.5}Ni_{0.3}Fe_{0.1}Mg_{0.1}O_2$, and the P3/P2/O3-composite. Reproduced with permission.[190] Copyright 2016, Wiley-VCH.

© 2019 WILEY-VCH Verlag GmbH & Co. KGaA, Weinheim

3.2.2. Layered–Spinel Category

*P2–*Fd$\bar{3}$*m Type*: Although P2 layered oxides have lower Na^+ transfer barrier than their O3-analog, their rate performance is still unsatisfactory. To address the issue, similar to strategy applied on the LS and LLS cathodes for LIBs, Zheng et al. integrated minor amount of *Fd*$\bar{3}$*m* spinel phase with P2-layered phase (**Figure 15**).[191] The *Fd*$\bar{3}$*m* spinel phase along the [011] zone axis shares structurally compatible cubic close-packed oxygen arrays with P2-phase along the[100] zone axis, which allows successful integration of the two phases into a composite. This heterostructured cathode in SIBs displays a capacity of 85 mAh g^{-1} at 1500 mA g^{-1}. This composite cathode was obtained by limiting Na source, which induced sodium-free spinel $Ni_{0.5}Co_{0.5}Mn_2O_4$. As a result, the P2–spinel composite cathode consists of active P2-layered cathode and inactive spinel oxides; the superior electronic and ionic conductivities of the spinel structure are the major reasons of the improved rate performance.

*O3–*Fd$\bar{3}$*m Category*: Recently, Xiong and co-workers successfully integrated spinel structure with O3-layered structure to obtain an intergrowth composite of $Na_{0.87}Li_{0.25}Ni_{0.4}Fe_{0.2}Mn_{0.4}O_{2+d}$ (LS–NFM) via Li^+ substitution and careful optimization of Na^+/Li^+ ratio.[192] It was reported that the O3 phase did not form at high Na^+ content, while formation of separate spinel phases is more favorable when the Li^+ content is too high. Rietveld refinement of the XRD pattern (**Figure 16**a) indicates that the composite consists 94% of the layered phase and 6% of a spinel phase. HRTEM image (Figure 16b) also reveals that the two phases integrate well in the nanoscale domain, which contributes to greater compatibility and connectivity of the two close-packed structures. Moreover, the layered and spinel structures are preserved after 50 cycles, which evidences good structural stability. As shown in Figure 16c,d, the LS–NFM cathode shows higher reversible capacity (112 vs 104 mAh g^{-1}), capacity retention (86% vs 70% after 100 cycles at 100 mA g^{-1}), and rate capability in comparison to the single-phase O3 layered cathode (NFM). The galvanostatic intermittent titration technique (Figure 16e,f) results also confirm that the Na^+ diffusion coefficient of LS–NMF is almost one order higher than that of NFM, which is a result of the direct channels between the 2D layered and 3D spinel phase.

3.2.3. Layered-Tunnel Category

Encouraged by the unique crystal structure and desirable electrochemical performances observed in orthorhombic $Na_{0.44}MnO_2$, the incorporation of layered cathodes with tunnel phase has also been explored. In 2014, Han et al. first prepared $NaAl_{0.1}Mn_{0.9}O_2$ containing both tunnel and layered crystal structures via Al substitution. This hybrid cathode shows enhanced cyclic performance and surface stability due to the strong Al—O bonds and synergetic effect between the layered and tunnel phases.[193] Given that P2-layered cathodes can deliver higher reversible capacity and rate performance than O3-phases in Mn-based cathode, Wu et al. prepared P2 layered-tunnel hybrid cathode via a coprecipitation method (**Figure 17**a).[159,194] In this study, although coexistence of the layered and tunnel structures is observed on specific particles, particles with only one crystal phase were commonly found. This can be attributed to the distinctly different oxygen arrangement of the two crystal phases. Despite so, the hybrid cathode still shows much better rate and cyclic performance compared to that of the pure P2-layered cathode (Figure 17b,c). A reversible capacity of 193.6 mAh g^{-1} is achieved by the layered-tunnel hybird with 70% of the capacity retained after 100 cycles of charge and discharge at 1 C. By contrast, the pure P2-layered cathode retains only 38% of its rechargeable capacity in the same condition. The superior rate capability of the hybrid (133.4 mAh g^{-1} at 8 C) also exceeds values of reported Mn-based cathodes. Combining density functional theory (DFT) calculations and reaction kinetic evaluation, the enhanced rate performance is explained by the current redistribution effect of the active materials, which helps to reduce polarization at high current density. A step further, Wu and co-workers studied the influence induced by substitution of Mn with Ni^{2+}, Cu^{2+}, Zr^{4+}, and optimized the crystal and elemental composition of a hybrid cathode (Figure 17d–f).[195–197] The investigation results suggest that Ni^{2+} only replaces the Mn ions within the layered structure, and the rest of Ni^{2+} forms into additional layered oxides of their own. Meanwhile, Cu^{2+} is doped into both the layered and tunnel structures, but extra layered oxides containing only Cu^{2+} also formed. Interestingly, the Zr^{4+} shows an equal tendency of doping into both phases, allowing the ratio of the crystal phases to be maintained, so that the effect of ion doping can be isolated for investigation. The substitution of Zr^{4+} for Mn^{4+} was discovered to increase the disorder in the TM layer and reduce the average unpaired electron density, which consequently enhances the rate capability. Moreover, the stronger Zr—O bond is also beneficial for structural stability, which resulted in better cyclic performance.

Later, Gao et al. prepared interface-rich P2–tunnel $Na_xCo_{0.1}Mn_{0.9}O_2$ composite ($0.44 < x < 0.7$) with Co substitution to address the Jahn–Teller distortion (**Figure 18**a,b).[198] With merits of the phase interface that provides extra channels for rapid Na^+ diffusion and active sites for charge storage, the hybrid cathode demonstrates a discharge capacity of 219 mAh g^{-1} at 0.1 C and 117 mAh g^{-1} at 5 C. Moreover, Guo and co-workers prepared layered-tunnel intergrowth $Na_{0.6}MnO_2$ by thermal polymerization and subsequent solid-state reaction (Figure 18c).[199] In situ XRD results suggest that the hybrid material achieves highly reversible structural evolution between P2–tunnel and OP4-tunnel phases over a wide voltage range, which leads to remarkable performances in energy density of 520.4 Wh kg^{-1}, discharge capacity of 198.2 mAh g^{-1}, and capacity retention of 85.1% after 100 cycles at 1 C (Figure 18d).

In the aforementioned reports, various types of P2–tunnel hybrid structures obtained by carefully controlling the preparation conditions are presented. However, it remains to be difficult to obtain composites with homogenously intergrown P2 and tunnel phases, which may be a result of the large differences in their crystal structures. Even with complex thermal polymerization method, microsections primarily consisting solely of P2 or tunnel structures cannot be avoided entirely. Despite so, the P2–tunnel composite still displays advantages of their components, showing enhanced current redistribution and phase transition reversibility. The tunnel structure with

© 2019 WILEY-VCH Verlag GmbH & Co. KGaA, Weinheim

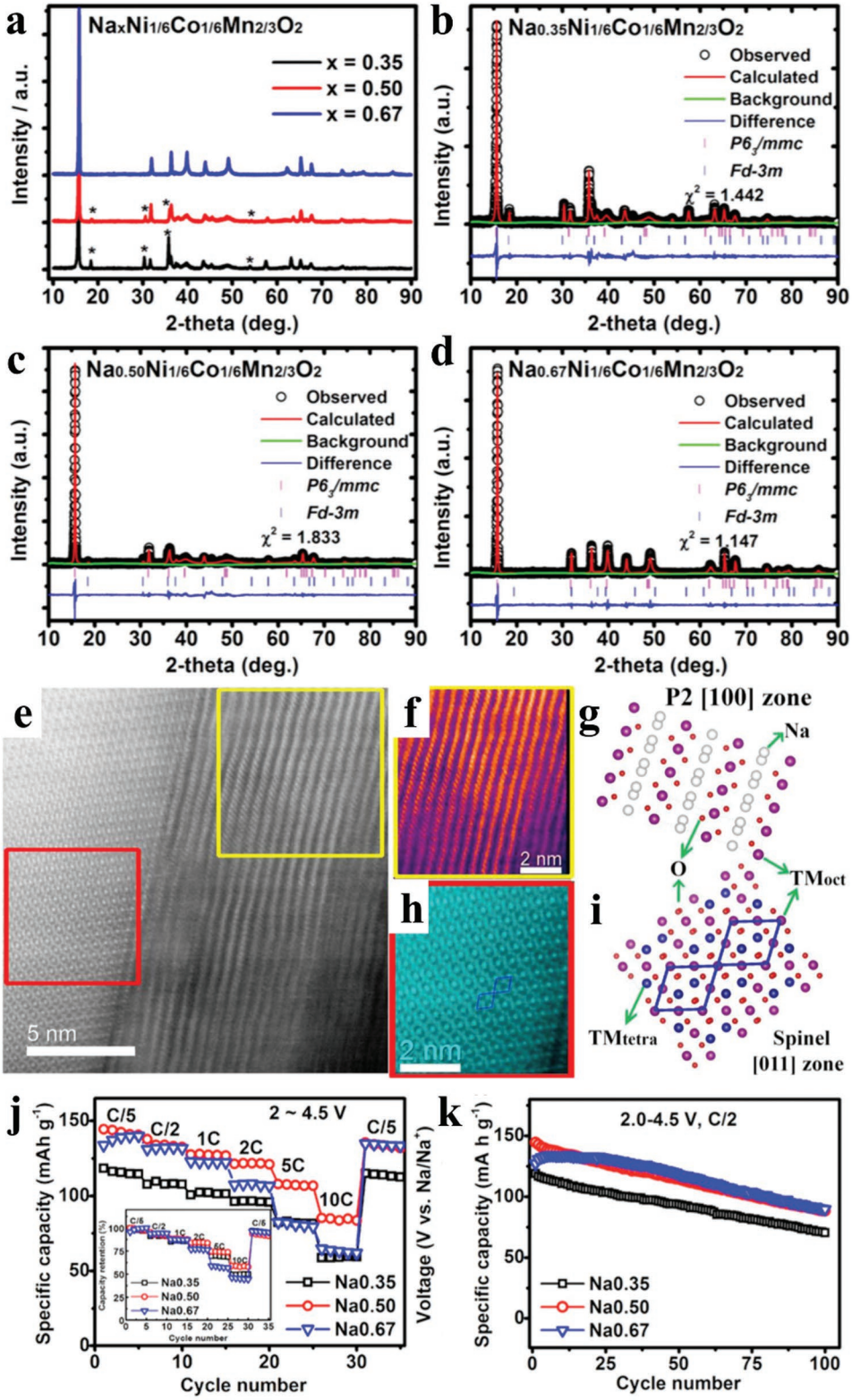

Figure 15. XRD patterns and corresponding detailed refinement of a) $Na_xNi_{1/6}Co_{1/6}Mn_{2/3}O_2$, b) $Na_{0.35}Ni_{1/6}Co_{1/6}Mn_{2/3}O_2$, c) $Na_{0.50}Ni_{1/6}Co_{1/6}Mn_{2/3}O_2$, and d) $Na_{0.67}Ni_{1/6}Co_{1/6}Mn_{2/3}O_2$. e) HAADF STEM images of the P2–$Fd\bar{3}m$ composite $Na_{0.50}Ni_{1/6}Co_{1/6}Mn_{2/3}O_2$. f) STEM image enlarged from the region encircled by yellow rectangle exhibiting lattice fringes of P2-layered structure and g) the corresponding atomic model of the[100] zone projection. h) STEM image enlarged from the region encircled by red rectangle reflecting the $Fd\bar{3}m$ spinel lattice fringes and i) the corresponding atomic model of the [011] zone projection. j) Rate capability and k) 0.5 C cyclic performance of $Na_xNi_{1/6}Co_{1/6}Mn_{2/3}O_2$. Reproduced with permission.[191] Copyright 2016, Electrochemical Society.

© 2019 WILEY-VCH Verlag GmbH & Co. KGaA, Weinheim

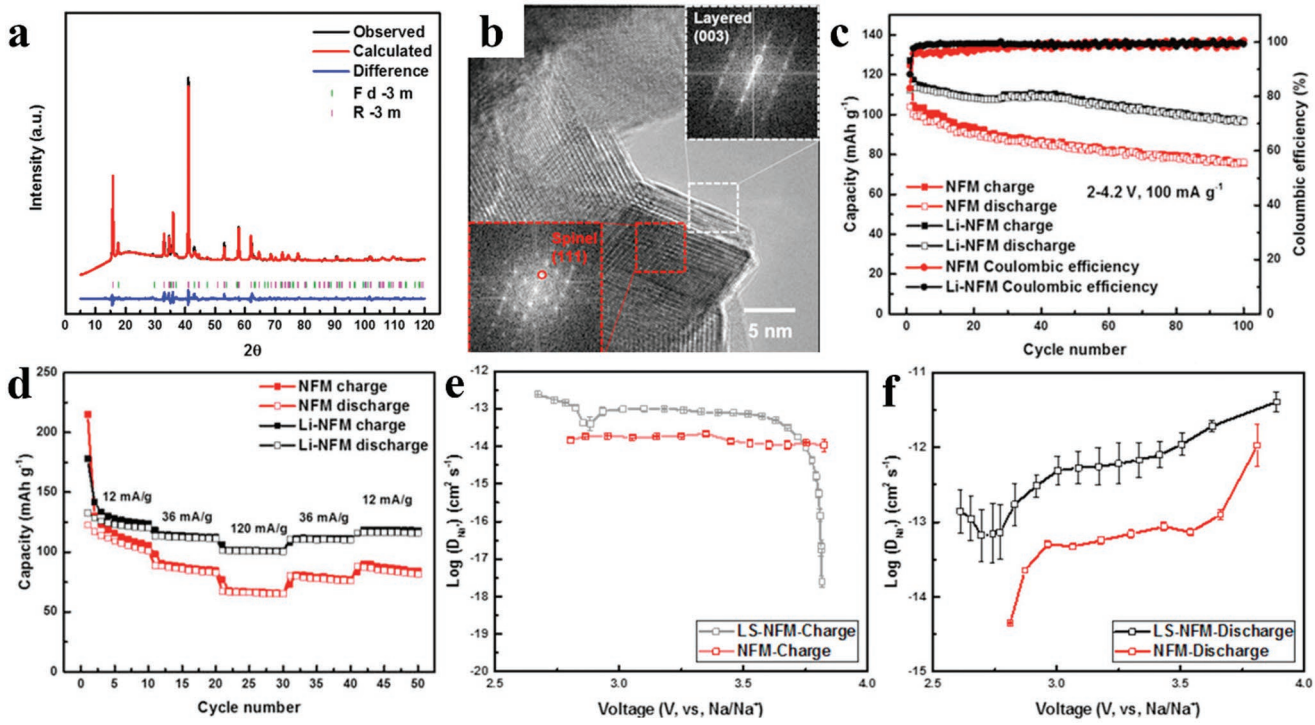

Figure 16. a) XRD pattern and Rietveld refinement of layered–tunneled $Na_{0.87}Li_{0.25}Ni_{0.4}Fe_{0.2}Mn_{0.4}O_{2+\delta}$ (LS–NFM); b) HRTEM image of LS–NFM (the insets are the corresponding FFT patterns of the encircle region). c) Cyclic performances and d) rate capabilities of LS–NFM and single-phase undoped NFM cathode; log D_{Na^+} plots during the e) charge and f) discharge process. Reproduced with permission.[192] Copyright 2018, American Chemical Society.

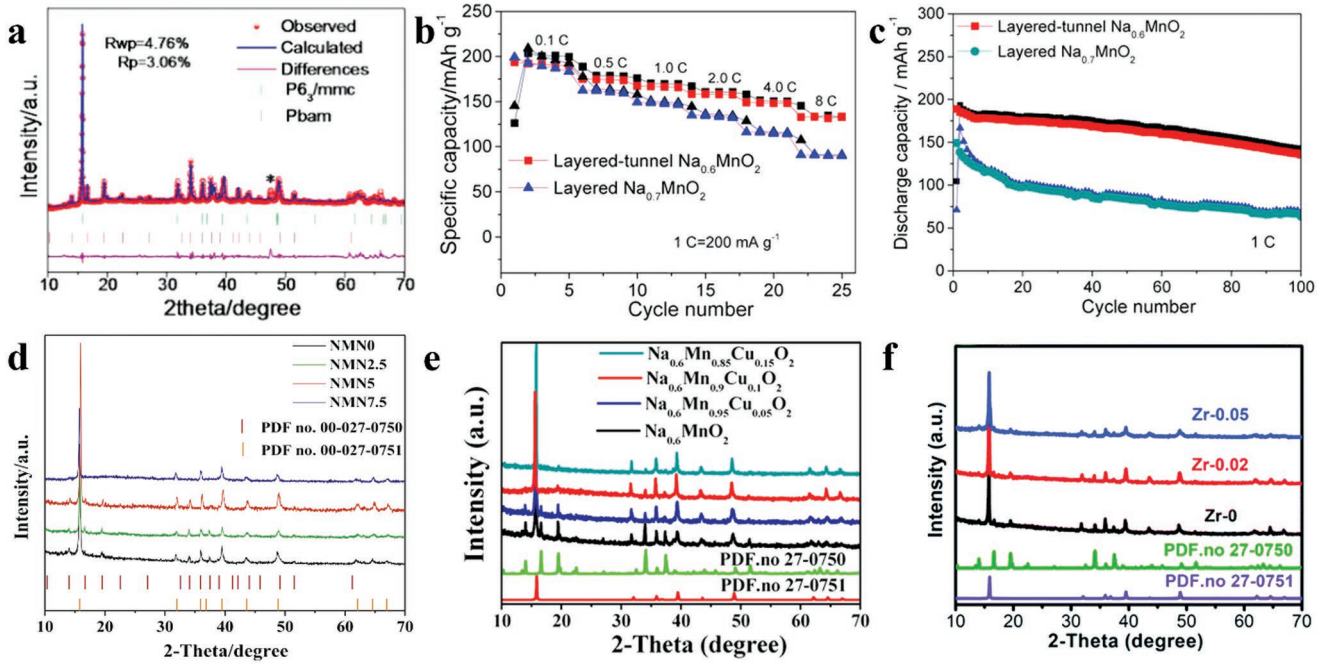

Figure 17. a) XRD pattern of layered–tunnel $Na_{0.6}MnO_2$. b) Rate and c) cyclic performance of layered $Na_{0.7}MnO_2$ and layered–tunnel $Na_{0.6}MnO_2$. Reproduced with permission.[194] Copyright 2017, American Chemical Society. d) XRD patterns of $Na_{0.6}Mn_{1-x}Ni_xO_2$, $x = 0$ (NMN0), 0.025 (NMN2.5), 0.05 (NMN5), 0.075 (NMN7.5). Reproduced with permission.[195] Copyright 2018, Elsevier. e) XRD patterns of $Na_{0.6}Mn_{1-x}Cu_xO_2$, $x = 0$, 0.05, 0.1, and 0.15. Reproduced with permission.[196] Copyright 2018, American Chemical Society. f) XRD patterns of $Na_{0.6}Mn_{1-x}Zr_xO_2$, $x = 0$ (Zr-0), 0.02 (Zr-0.02), and 0.05 (Zr-0.05). Reproduced with permission.[197] Copyright 2018, Royal Society of Chemistry.

© 2019 WILEY-VCH Verlag GmbH & Co. KGaA, Weinheim

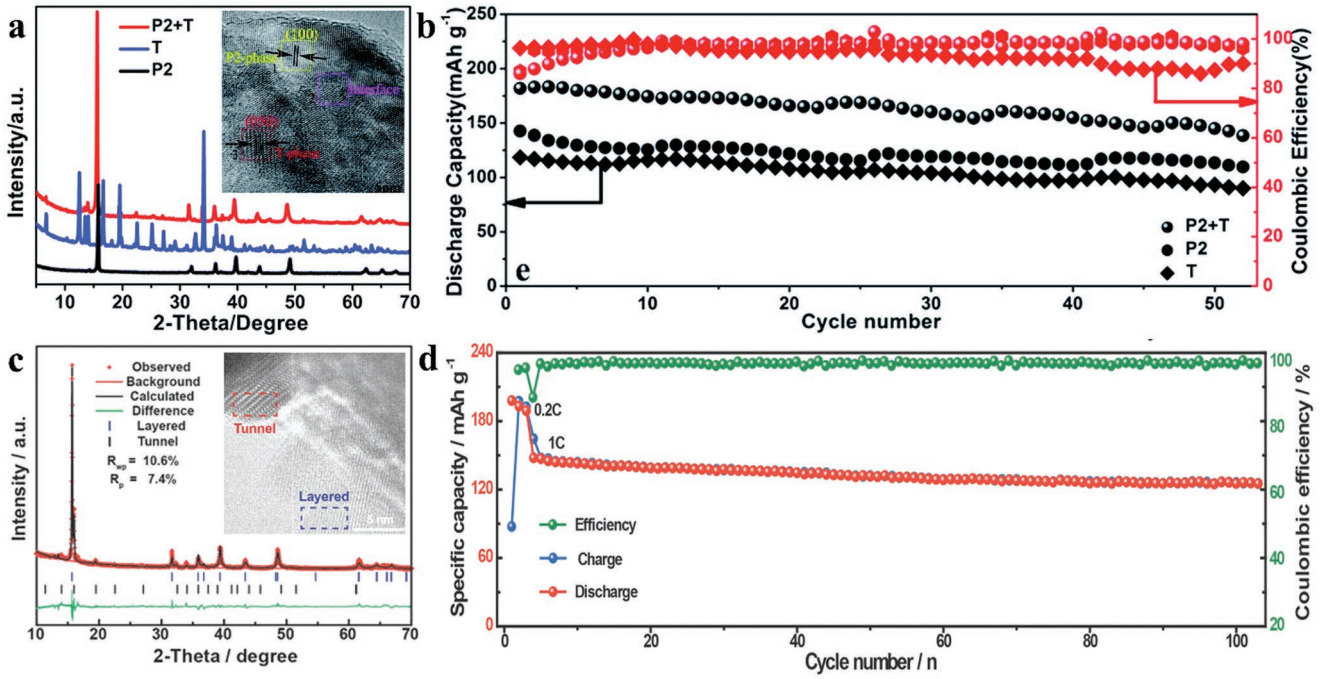

Figure 18. a) XRD patterns, b) cyclic performances of pristine P2-$Na_{0.7}Co_{0.1}Mn_{0.9}O_2$, T-$Na_{0.44}Co_{0.1}Mn_{0.9}O_2$, and P2+T-$Na_xCo_{0.1}Mn_{0.9}O_2$; inset: HRTEM image of the P2+T-material. Reproduced with permission.[198] Copyright 2018, Royal Society of Chemistry. c) XRD pattern and Rietveld refinement plots of layered–tunnel intergrowth sample; inset: HRTEM image of the layered–tunnel intergrowth sample; d) cyclic performance of layered–tunnel intergrowth electrode at 1 C. Reproduced with permission.[199] Copyright 2018, Wiley-VCH.

better electronic/ion conductivity bears more current than the layered structure during cycling, and may serve as fast ion conductor after it is fully charged/discharged. Their highly reversible phase transition during the electrochemical process also reveals better structure stability and feasible Na^+ diffusion.

4. Conclusions and Future Perspectives

From intrinsic electrochemical properties, morphology, crystal structure to representative synthetic methodology, the relevant research progresses of heterostructured cathode materials for LIBs and SIBs are presented. Benefiting from the synergistic effect between each component, the electrochemical performances of these composites are significantly optimized, demonstrating high capacity, superb rate, and cyclic performance. These multiphases heterostructured cathodes belong to the frontier of the current battery technology with commercial products such as Yuasa eNi TIME and Panasonic (Sanyo) eneloop launched and popularized worldwide.[26] Nevertheless, several aspects of the heterostructured cathodes are still not comprehensively understood and challenges remain to be addressed. First, continuous efforts are still required to further decipher the voltage and capacity fading mechanism. A complete understanding of the process would allow for formulation of a guideline to fine-tune compositions in heterostructured cathode materials, which is necessary for pursuing complex multiphase cathodes with optimal balance between initial coulombic efficiency, specific capacity, operation voltage, thermal stability, cost, and environmental impact. For example, the guideline may then serve as the bases for combining ternary LLS with $LiFePO_4$ to realize quaternary cathodes with performances that are one step higher than the components. Detailed investigations on structural transformation and ion/electron diffusions of the crystal interfaces may also provide insights for further improvement. Second, the widely applied carbonate-based electrolytes are unstable in the high potential required for proper activation of Li_2MnO_3-containing binary LL or ternary LLS composites. Side reactions between $LiPF_6$ containing electrolyte and oxygen radicals generated during cycling may also cause severe corrosion on the cathode surface. As such, exploration of safe and stable electrolytes capable of withstanding the widened operation voltage windows is another ongoing research target in the field. Third, advancement of characterization techniques with elevated resolution is necessary for detecting the crystal structural evolution, synthetic route influence, and electrochemical behaviors of the heterostructured cathodes at the atomic scale. New knowledge about the battery systems obtained from these technologies will likely inspire the next generation of cathodes for LIBs and SIBs that further advance the applications of practical large-scale grid storage and renewable energy.

Acknowledgements

Y.-P.D., Z.-G.W., R.L., and Y.J. contributed equally to this work. The authors wish to acknowledge the support provided by Natural Sciences and Engineering Research Council of Canada (NSERC), University of Waterloo, Waterloo Institute for Nanotechnology and by the National Natural Science Foundation of China (Grant No. 21805198). Y.-P.D. acknowledges the support of the China Scholarship Council (CSC).

© 2019 WILEY-VCH Verlag GmbH & Co. KGaA, Weinheim

Conflict of Interest

The authors declare no conflict of interest.

Keywords

cathode material, crystal structure, heterostructure, lithium-ion batteries, sodium-ion batteries

Received: December 1, 2018
Revised: January 31, 2019
Published online:

[1] J. B. Goodenough, *Nat. Electron.* **2018**, *1*, 204.
[2] M. S. Whittingham, *Chem. Rev.* **2004**, *104*, 4271.
[3] B. Dunn, H. Kamath, J. M. Tarascon, *Science* **2011**, *334*, 928.
[4] P. G. Bruce, S. A. Freunberger, L. J. Hardwick, J.-M. Tarascon, *Nat. Mater.* **2012**, *11*, 19.
[5] M. Winter, R. J. Brodd, What Are Batteries, *Chem. Rev.* **2004**, *104*, 4245.
[6] Y. Li, J. Lu, *ACS Energy Lett.* **2017**, *2*, 1370.
[7] Y. P. Deng, Y. Jiang, D. Luo, J. Fu, R. Liang, S. Cheng, Z. Bai, Y. Liu, W. Lei, L. Yang, J. Zhu, Z. Chen, *ACS Energy Lett.* **2017**, *2*, 2706.
[8] W. Lei, Y. P. Deng, G. Li, Z. P. Cano, X. Wang, D. Luo, Y. Liu, D. Wang, Z. Chen, *ACS Catal.* **2018**, *8*, 2464.
[9] G. Li, W. Lei, D. Luo, Y. P. Deng, D. Wang, Z. Chen, *Adv. Energy Mater.* **2017**, *8*, 1702381.
[10] G. Li, W. Lei, D. Luo, Y. P. Deng, Z. Deng, D. Wang, A. Yu, Z. Chen, *Energy Environ. Sci.* **2018**, *11*, 2372.
[11] Y. Jiang, Y. P. Deng, J. Fu, D. U. Lee, R. Liang, Z. P. Cano, Y. Liu, Z. Bai, S. Hwang, L. Yang, D. Su, W. Chu, Z. Chen, *Adv. Energy Mater.* **2018**, *8*, 1870068.
[12] Y. Jiang, Y. P. Deng, J. Fu, D. U. Lee, R. Liang, Z. P. Cano, Y. Liu, Z. Bai, S. Hwang, L. Yang, D. Su, W. Chu, Z. Chen, *Adv. Energy Mater.* **2018**, *8*, 1702900.
[13] D. Kundu, E. Talaie, V. Duffort, L. F. Nazar, *Angew. Chem., Int. Ed.* **2015**, *54*, 3431.
[14] M. D. Slater, D. Kim, E. Lee, C. S. Johnson, Sodium-Ion Batteries, *Adv. Funct. Mater.* **2013**, *23*, 947.
[15] P. K. Nayak, L. Yang, W. Brehm, *Angew. Chem., Int. Ed.* **2018**, *57*, 102.
[16] D. Luo, Y. P. Deng, X. Wang, G. Li, J. Wu, J. Fu, W. Lei, R. Liang, Y. Liu, Y. Ding, A. Yu, Z. Chen, *ACS Nano* **2017**, *11*, 11521.
[17] Y. Zhu, X. Han, Y. Xu, Y. Liu, S. Zheng, K. Xu, L. Hu, *ACS Nano* **2013**, *7*, 6378.
[18] J. I. Lee, K. T. Lee, J. Cho, J. Kim, N. S. Choi, S. Park, *Angew. Chem., Int. Ed.* **2012**, *51*, 2767.
[19] Y. Son, Y. Son, M. Choi, M. Ko, S. Chae, N. Park, J. Cho, *Nano Lett.* **2015**, *15*, 6914.
[20] M.-H. Park, M. G. Kim, J. Joo, K. Kim, J. Kim, S. Ahn, Y. Cui, J. Cho, *Nano Lett.* **2009**, *9*, 3844.
[21] Y. Wen, K. He, Y. Zhu, F. Han, Y. Xu, I. Matsuda, Y. Ishii, J. Cumings, C. Wang, *Nat. Commun.* **2014**, *5*, 4033.
[22] W. Lei, W. Xiao, J. Li, G. Li, Z. Wu, C. Xuan, D. Luo, Y. P. Deng, D. Wang, Z. Chen, *ACS Appl. Mater. Interfaces* **2017**, *9*, 28604.
[23] O. K. Park, Y. Cho, S. Lee, H.-C. Yoo, H.-K. Song, J. Cho, *Energy Environ. Sci.* **2011**, *4*, 1621.
[24] Y. Jiang, R. Tian, H. Liu, J. Chen, X. Tan, L. Zhang, G. Liu, H. Wang, L. Sun, W. Chu, *Nano Res.* **2015**, *8*, 3803.
[25] W. Li, B. Song, A. Manthiram, *Chem. Soc. Rev.* **2017**, *46*, 3006.
[26] L. Wang, J. L. Shi, H. Su, G. Li, M. Zubair, Y. G. Guo, H. Yu, *Small* **2018**, *14*, 1800887.
[27] P. Roziera, J. M. Tarascon, *J. Electrochem. Soc.* **2015**, *162*, A2490.
[28] Y. P. Deng, F. Fu, Z. G. Wu, T. Zhang, Z. W. Yin, S. J. Zhang, J. T. Li, L. Huang, S. G. Sun, *ChemElectroChem* **2016**, *3*, 2027.
[29] X. Miao, Y. Yan, C. Wang, L. Cui, J. Fang, G. Yang, *J. Power Sources* **2014**, *247*, 219.
[30] M. M. Thackeray, S. H. Kang, C. S. Johnson, J. T. Vaughey, R. Benedek, S. A. Hackney, *J. Mater. Chem.* **2007**, *17*, 3053.
[31] H. Su, H. Yu, *Small Methods* **2018**, *114*, 1800205.
[32] A. R. Armstrong, P. G. Bruce, *Nature* **1996**, *381*, 499.
[33] R. Chen, T. Zhao, X. Zhang, L. Li, F. Wu, *Nanoscale Horiz.* **2016**, *1*, 423.
[34] P. K. Nayak, E. M. Erickson, F. Schipper, T. R. Penki, N. Munichandraiah, P. Adelhelm, H. Sclar, F. Amalraj, B. Markovsky, D. Aurbach, *Adv. Energy Mater.* **2018**, *8*, 1702397.
[35] J. R. Croy, M. Balasubramanian, K. G. Gallagher, A. K. Burrell, *Acc. Chem. Res.* **2015**, *48*, 2813.
[36] Q. Wang, C. H. Shen, S. Y. Shen, Y. F. Xu, C. G. Shi, L. Huang, J. T. Li, S. G. Sun, *ACS Appl. Mater. Interfaces* **2017**, *9*, 24731.
[37] H. Yu, Y. Qian, M. Otani, D. Tang, S. Guo, Y. Zhu, H. Zhou, *Energy Environ. Sci.* **2014**, *7*, 1068.
[38] W. Liu, P. Oh, X. Liu, M. J. Lee, W. Cho, S. Chae, Y. Kim, J. Cho, *Angew. Chem., Int. Ed.* **2015**, *54*, 4440.
[39] P. Kalyani, S. Chitra, T. Mohan, S. Gopukumar, *J. Power Sources* **1999**, *80*, 103.
[40] R. Wang, X. He, L. He, F. Wang, R. Xiao, L. Gu, H. Li, L. Chen, *Adv. Energy Mater.* **2013**, *3*, 1358.
[41] Y. Shin, H. Ding, K. A. Persson, *Chem. Mater.* **2016**, *28*, 2081.
[42] M. H. A. Robert Armstrong, P. Novak, C. S. Johnson, M. M. T. Sun-Ho Kang, *J. Am. Chem. Soc.* **2006**, *128*, 8694.
[43] P. Yan, L. Xiao, J. Zheng, Y. Zhou, Y. He, X. Zu, S. X. Mao, J. Xiao, F. Gao, J.-G. Zhang, C.-M. Wang, *Chem. Mater.* **2015**, *27*, 975.
[44] M. M. Thackeray, P. J. Johnson, L. A. d. Picciotto, P. G. Bruce, J. B. Goodenough, *Mater. Res. Bull.* **1984**, *19*, 179.
[45] M. M. Thackeray, W. I. F. David, P. G. Bruce, J. B. Goodenough, *Mater. Res. Bull.* **1983**, *18*, 461.
[46] Q. Zhao, Z. Yan, C. Chen, J. Chen, *Chem. Rev.* **2017**, *117*, 10121.
[47] M. M. Thackeray, *Prog. Solid State Chem.* **1997**, *25*, 1.
[48] H. Li, Z. Wang, L. Chen, X. Huang, *Adv. Mater.* **2009**, *21*, 4593.
[49] S. Lee, G. Yoon, M. Jeong, M. J. Lee, K. Kang, J. Cho, *Angew. Chem., Int. Ed.* **2015**, *54*, 1153.
[50] L. Guohua, H. Ikuto, T. Uchida, M. Wakihara, *J. Electrochem. Soc.* **1996**, *143*, 178.
[51] E. S. Lee, K. W. Nam, E. Hu, A. Manthiram, *Chem. Mater.* **2012**, *24*, 3610.
[52] T. Takada, H. Hayakawa, E. Akiba, *J. Solid State Chem.* **1995**, *115*, 420.
[53] F. Fu, G. L. Xu, Q. Wang, Y. P. Deng, X. Li, J. T. Li, L. Huang, S. G. Sun, *J. Mater. Chem. A* **2013**, *1*, 3860.
[54] L. Zhou, D. Zhao, X. Lou, *Angew. Chem., Int. Ed.* **2012**, *51*, 239.
[55] Y. L. Ding, X. B. Zhao, J. Xie, G. S. Cao, T. J. Zhu, H.-M. Yu, C. Y. Sun, *J. Mater. Chem.* **2011**, *21*, 9475.
[56] M. Okubo, Y. Mizuno, H. Yamada, J. Kim, E. Hosono, H. Zhou, T. Kudo, I. Honma, *ACS Nano* **2010**, *4*, 741.
[57] G. Ma, S. Li, W. Zhang, Z. Yang, S. Liu, X. Fan, F. Chen, Y. Tian, W. Zhang, S. Yang, M. Li, *Angew. Chem., Int. Ed.* **2016**, *55*, 3667.
[58] Y. Wu, C. Cao, Y. Zhu, J. Li, L. Wang, *J. Mater. Chem. A* **2015**, *3*, 15523.
[59] X. W. D. Lou, L. A. Archer, Z. Yang, *Adv. Mater.* **2008**, *20*, 3987.
[60] Y. K. Sun, S. T. Myung, B. C. Park, J. Prakash, I. Belharouak, K. Amine, *Nat. Mater.* **2009**, *8*, 320.
[61] R. P. Qing, J. L. Shi, D. D. Xiao, X. D. Zhang, Y. X. Yin, Y. B. Zhai, L. Gu, Y. G. Guo, *Adv. Energy Mater.* **2016**, *6*, 1501914.
[62] S. N. Lim, J. Y. Seo, D. S. Jung, W. Ahn, H. S. Song, S. H. Yeon, S. B. Park, *J. Alloys Compd.* **2015**, *623*, 55.
[63] J. Wang, W. Lin, B. Wu, J. Zhao, *Electrochim. Acta* **2014**, *145*, 245.

© 2019 WILEY-VCH Verlag GmbH & Co. KGaA, Weinheim

[64] J. Tian, Y. Su, F. Wu, S. Xu, F. Chen, R. Chen, Q. Li, J. Li, F. Sun, S. Chen, *ACS Appl. Mater. Interfaces* **2016**, *8*, 582.
[65] Y. Cho, S. Lee, Y. Lee, T. Hong, J. Cho, *Adv. Energy Mater.* **2011**, *1*, 821.
[66] J. Zhang, Z. Yang, R. Gao, L. Gu, Z. Hu, X. Liu, *ACS Appl. Mater. Interfaces* **2017**, *9*, 29794.
[67] Y. D. Xu, W. Xiang, Z. G. Wu, C. L. Xu, Y. C. Li, X. D. Guo, G. P. Lv, X. Peng, B. H. Zhong, *Electrochim. Acta* **2018**, *268*, 358.
[68] R. Gu, Z. Ma, T. Cheng, Y. Lyu, A. Nie, B. Guo, *ACS Appl. Mater. Interfaces* **2018**, *10*, 31271.
[69] J. H. Song, A. Kapylou, H. S. Choi, B. Y. Yu, E. Matulevich, S. H. Kang, *J. Power Sources* **2016**, *313*, 65.
[70] F. Wu, Z. Wang, Y. Su, N. Yan, L. Bao, S. Chen, *J. Power Sources* **2014**, *247*, 20.
[71] F. Fu, Q. Wang, Y. P. Deng, C. H. Shen, X. X. Peng, L. Huang, S. G. Sun, *J. Mater. Chem. A* **2015**, *3*, 5197.
[72] N. Koichi, S. Chie, Y. Shoji, *Chem. Lett.* **1997**, *26*, 725.
[73] A. Manthiram, J. C. Knight, S. T. Myung, S. M. Oh, Y. K. Sun, *Adv. Energy Mater.* **2016**, *6*, 1501010.
[74] T. Zhang, J. T. Li, J. Liu, Y. P. Deng, Z. G. Wu, Z. W. Yin, J. H. Wu, L. Huang, S. G. Sun, *ChemElectroChem* **2016**, *3*, 98.
[75] K. Numata, S. Yamanaka, *Solid State Ionics* **1999**, *118*, 117.
[76] S. Kim, M. Aykol, V. I. Hegde, Z. Lu, S. Kirklin, J. R. Croy, M. M. Thackeray, C. Wolverton, *Energy Environ. Sci.* **2017**, *10*, 2201.
[77] N. Yabuuchi, K. Yoshii, S. T. Myung, I. Nakai, S. Komaba, *J. Am. Chem. Soc.* **2011**, *133*, 4404.
[78] M. Sathiya, A. M. Abakumov, D. Foix, G. Rousse, K. Ramesha, M. Saubanere, M. L. Doublet, H. Vezin, C. P. Laisa, A. S. Prakash, D. Gonbeau, G. VanTendeloo, J. M. Tarascon, *Nat. Mater.* **2015**, *14*, 230.
[79] J. Li, J. Camardese, R. Shunmugasundaram, S. Glazier, Z. Lu, J. R. Dahn, *Chem. Mater.* **2015**, *27*, 3366.
[80] A. Vu, L. K. Walker, J. Bareño, A. K. Burrell, I. Bloom, *J. Power Sources* **2015**, *280*, 155.
[81] D. Peralta, J. F. Colin, A. Boulineau, L. Simonin, F. Fabre, J. Bouvet, P. Feydi, M. Chakir, M. Chapuis, S. Patoux, *J. Power Sources* **2015**, *280*, 687.
[82] Y. Wu, C. Ma, J. Yang, Z. Li, L. F. Allard, C. Liang, M. Chi, *J. Mater. Chem. A* **2015**, *3*, 5385.
[83] X. Yu, Y. Lyu, L. Gu, H. Wu, S. M. Bak, Y. Zhou, K. Amine, S. N. Ehrlich, H. Li, K. W. Nam, X. Q. Yang, *Adv. Energy Mater.* **2014**, *4*, 1300950.
[84] J. Zheng, P. Xu, M. Gu, J. Xiao, N. D. Browning, P. Yan, C. Wang, J. G. Zhang, *Chem. Mater.* **2015**, *27*, 1381.
[85] A. Boulineau, L. Simonin, J. F. Colin, C. Bourbon, S. Patoux, *Nano Lett.* **2013**, *13*, 3857.
[86] D. Mohanty, S. Kalnaus, R. A. Meisner, K. J. Rhodes, J. Li, E. A. Payzant, D. L. Wood, C. Daniel, *J. Power Sources* **2013**, *229*, 239.
[87] M. G. Kim, M. Jo, Y. S. Hong, J. Cho, *Chem. Commun.* **2009**, 218.
[88] G. Z. Wei, X. Lu, F. S. Ke, L. Huang, J. T. Li, Z. X. Wang, Z. Y. Zhou, S. G. Sun, *Adv. Mater.* **2010**, *22*, 4364.
[89] L. Chen, Y. Su, S. Chen, N. Li, L. Bao, W. Li, Z. Wang, M. Wang, F. Wu, *Adv. Mater.* **2014**, *26*, 6756.
[90] L. Zhang, W. Boronga, L. Ning, W. Feng, *Electrochim. Acta* **2014**, *118*, 67.
[91] D. H. Park, S. T. Lim, S. J. Hwang, C. S. Yoon, Y. K. Sun, J. H. Choy, *Adv. Mater.* **2005**, *17*, 2834.
[92] Y. Xiang, J. Li, X. Wu, Z. Liu, L. Xiong, Z. He, Z. Yin, *Ceram. Int.* **2016**, *42*, 8833.
[93] Z. Tang, X. Li, Z. Wang, *Ionics* **2013**, *19*, 1495.
[94] X. Feng, Y. Gao, L. Ben, Z. Yang, Z. Wang, L. Chen, *J. Power Sources* **2016**, *317*, 74.
[95] D. Xie, G. Li, Q. Li, C. Fu, J. Fan, L. Li, *Electrochim. Acta* **2016**, *196*, 505.
[96] H. Liu, C. Du, G. Yin, B. Song, P. Zuo, X. Cheng, Y. Ma, Y. Gao, *J. Mater. Chem. A* **2014**, *2*, 15640.
[97] F. Wu, X. Zhang, T. Zhao, L. Li, M. Xie, R. Chen, *ACS Appl. Mater. Interfaces* **2015**, *7*, 3773.
[98] Y. K. Sun, M. J. Lee, C. S. Yoon, J. Hassoun, K. Amine, B. Scrosati, *Adv. Mater.* **2012**, *24*, 1192.
[99] Z. Wang, S. Luo, J. Ren, D. Wang, X. Qi, *Appl. Surf. Sci.* **2016**, *370*, 437.
[100] S. T. Myung, K. Izumi, S. Komaba, Y. K. Sun, H. Yashiro, A. N. Kumagai, *Chem. Mater.* **2005**, *117*, 3695.
[101] W. Yuan, H. Z. Zhang, Q. Liu, G. R. Li, X. P. Gao, *Electrochim. Acta* **2014**, *135*, 199.
[102] Z. Chen, Y. Qin, K. Amine, Y. K. Sun, *J. Mater. Chem.* **2010**, *20*, 7606.
[103] J. Ma, B. Li, L. An, H. Wei, X. Wang, P. Yu, D. Xia, *J. Power Sources* **2015**, *277*, 393.
[104] Z. Wang, E. Liu, C. He, C. Shi, J. Li, N. Zhao, *J. Power Sources* **2013**, *236*, 25.
[105] C. Wu, X. Fang, X. Guo, Y. Mao, J. Ma, C. Zhao, Z. Wang, L. Chen, *J. Power Sources* **2013**, *231*, 44.
[106] J. Z. Kong, C. Ren, Y. X. Jiang, F. Zhou, C. Yu, W. P. Tang, H. Li, S. Y. Ye, J. X. Li, *J. Solid State Electrochem.* **2016**, *20*, 1435.
[107] J. M. Zheng, Z. R. Zhang, X. B. Wu, Z. X. Dong, Z. Zhu, Y. Yang, *J. Electrochem. Soc.* **2008**, *155*, A775.
[108] S. T. Myung, K. S. Lee, C. S. Yoon, Y. K. Sun, K. Amine, H. Yashiro, *J. Phys. Chem. C* **2010**, *114*, 4710.
[109] S. H. Kang, W. S. Yoon, K. W. Nam, X. Q. Yang, D. P. Abraham, *J. Mater. Sci.* **2008**, *43*, 4701.
[110] J. Gao, J. Kim, A. Manthiram, *Electrochem. Commun.* **2009**, *11*, 84.
[111] J. Gao, A. Manthiram, *J. Power Sources* **2009**, *191*, 644.
[112] B. Qiu, J. Wang, Y. Xia, Z. Wei, S. Han, Z. Liu, *J. Power Sources* **2014**, *267*, 517.
[113] R. Shunmugasundaram, R. Senthil Arumugam, J. R. Dahn, *Chem. Mater.* **2015**, *27*, 757.
[114] F. Fu, Y. P. Deng, C. H. Shen, G. L. Xu, X. X. Peng, Q. Wang, Y. F. Xu, J. C. Fang, L. Huang, S. G. Sun, *Electrochem. Commun.* **2014**, *44*, 54.
[115] Q. Li, G. Li, C. Fu, D. Luo, J. Fan, L. Li, *ACS Appl. Mater. Interfaces* **2014**, *6*, 10330.
[116] J. Zheng, M. Gu, J. Xiao, P. Zuo, C. Wang, J. G. Zhang, *Nano Lett.* **2013**, *13*, 3824.
[117] S. Zhang, H. Gu, H. Pan, S. Yang, W. Du, X. Li, M. Gao, Y. Liu, M. Zhu, L. Ouyang, D. Jian, F. Pan, *Adv. Energy Mater.* **2017**, *7*, 1601066.
[118] T. Zhang, J. T. Li, J. Liu, Y. P. Deng, Z. G. Wu, Z. W. Yin, D. Guo, L. Huang, S. G. Sun, *Chem. Commun.* **2016**, *52*, 4683.
[119] S. Myeong, W. Cho, W. Jin, J. Hwang, M. Yoon, Y. Yoo, G. Nam, H. Jang, J. G. Han, N. S. Choi, M. G. Kim, J. Cho, *Nat. Commun.* **2018**, *9*, 3285.
[120] C. H. Shen, S. Y. Shen, F. Fu, C. G. Shi, H. Y. Zhang, M. J. Pierre, H. Su, Q. Wang, B. B. Xu, L. Huang, J. T. Li, S. G. Sun, *J. Mater. Chem. A* **2015**, *3*, 12220.
[121] C. H. Shen, Q. Wang, F. Fu, L. Huang, Z. Lin, S. Y. Shen, H. Su, X. M. Zheng, B. B. Xu, J. T. Li, S. G. Sun, *ACS Appl. Mater. Interfaces* **2014**, *6*, 5516.
[122] J. Hong, H. D. Lim, M. Lee, S. W. Kim, H. Kim, S. T. Oh, G. C. Chung, K. Kang, *Chem. Mater.* **2012**, *24*, 2692.
[123] E. Hu, Y. Lyu, H. L. Xin, J. Liu, L. Han, S. M. Bak, J. Bai, X. Yu, H. Li, X. Q. Yang, *Nano Lett.* **2016**, *16*, 5999.
[124] J. T. Li, Z. Y. Wu, Y. Q. Lu, Y. Zhou, Q. S. Huang, L. Huang, S. G. Sun, *Adv. Energy Mater.* **2017**, *7*, 1701185.
[125] S. J. Zhang, Y. P. Deng, Q. H. Wu, Y. Zhou, J. T. Li, Z. Y. Wu, Z. W. Yin, Y. Q. Lu, C. H. Shen, L. Huang, S. G. Sun, *ChemElectroChem* **2018**, *5*, 1321.
[126] F. Zheng, C. Yang, X. Xiong, J. Xiong, R. Hu, Y. Chen, M. Liu, *Angew. Chem., Int. Ed.* **2015**, *54*, 13058.

© 2019 WILEY-VCH Verlag GmbH & Co. KGaA, Weinheim

[127] W. Liu, P. Oh, X. Liu, S. Myeong, W. Cho, J. Cho, *Adv. Energy Mater.* **2015**, *5*, 1500274.
[128] P. K. Nayak, J. Grinblat, M. Levi, E. Levi, S. Kim, J. W. Choi, D. Aurbach, *Adv. Energy Mater.* **2016**, *6*, 1502398.
[129] P. E. Pearce, A. J. Perez, G. Rousse, M. Saubanere, D. Batuk, D. Foix, E. McCalla, A. M. Abakumov, G. Van Tendeloo, M. L. Doublet, J. M. Tarascon, *Nat. Mater.* **2017**, *16*, 580.
[130] A. J. Perez, Q. Jacquet, D. Batuk, A. Iadecola, M. Saubanère, G. Rousse, D. Larcher, H. Vezin, M.-L. Doublet, J.-M. Tarascon, *Nat. Energy* **2017**, *2*, 954.
[131] S. Kang, H. Qin, Y. Fang, X. Li, Y. Wang, *Electrochim. Acta* **2014**, *144*, 22.
[132] X. Zhang, Y. Yin, Y. Hu, Q. Wu, Y. Bai, *Electrochim. Acta* **2016**, *193*, 96.
[133] J. L. Shi, J. N. Zhang, M. He, X. D. Zhang, Y. X. Yin, H. Li, Y. G. Guo, L. Gu, L. J. Wan, *ACS Appl. Mater. Interfaces* **2016**, *8*, 20138.
[134] Y. P. Deng, F. Fu, Z. G. Wu, Z. W. Yin, T. Zhang, J. T. Li, L. Huang, S. G. Sun, *J. Mater. Chem. A* **2016**, *4*, 257.
[135] F. Wu, N. Li, Y. Su, H. Shou, L. Bao, W. Yang, L. Zhang, R. An, S. Chen, *Adv. Mater.* **2013**, *25*, 3722.
[136] Y. P. Deng, Z. W. Yin, Z. G. Wu, S. J. Zhang, F. Fu, T. Zhang, J. T. Li, L. Huang, S. G. Sun, *ACS Appl. Mater. Interfaces* **2017**, *9*, 21065.
[137] B. Song, H. Liu, Z. Liu, P. Xiao, M. O. Lai, L. Lu, *Sci. Rep.* **2013**, *3*, 3094.
[138] S. Wang, Y. Wu, Y. Li, J. Zheng, J. Yang, Y. Yang, *Electrochim. Acta* **2014**, *133*, 100.
[139] S. K. Jeong, J. S. Shin, K. S. Nahm, T. Prem Kumar, A. M. Stephan, *Mater. Chem. Phys.* **2008**, *111*, 213.
[140] F. Wu, N. Li, Y. Su, L. Zhang, L. Bao, J. Wang, L. Chen, Y. Zheng, L. Dai, J. Peng, S. Chen, *Nano Lett.* **2014**, *14*, 3550.
[141] Q. Xia, X. Zhao, M. Xu, Z. Ding, J. Liu, L. Chen, D. G. Ivey, W. Wei, *J. Mater. Chem. A* **2015**, *3*, 3995.
[142] J. Zhao, R. Huang, W. Gao, J.-M. Zuo, X. F. Zhang, S. T. Misture, Y. Chen, J. V. Lockard, B. Zhang, S. Guo, M. R. Khoshi, K. Dooley, H. He, Y. Wang, *Adv. Energy Mater.* **2015**, *5*, 1401937.
[143] J. Zheng, M. Gu, J. Xiao, B. J. Polzin, P. Yan, X. Chen, C. Wang, J. G. Zhang, *Chem. Mater.* **2014**, *26*, 6320.
[144] X. Bian, Q. Fu, H. Qiu, F. Du, Y. Gao, L. Zhang, B. Zou, G. Chen, Y. Wei, *Chem. Mater.* **2015**, *27*, 5745.
[145] D. Luo, G. Li, C. Fu, J. Zheng, J. Fan, Q. Li, L. Li, *Adv. Energy Mater.* **2014**, *4*, 1400062.
[146] Y. Pei, C. Y. Xu, Y. C. Xiao, Q. Chen, B. Huang, B. Li, S. Li, L. Zhen, G. Cao, *Adv. Funct. Mater.* **2017**, *27*, 1604349.
[147] D. Wang, R. Yu, X. Wang, L. Ge, X. Yang, *Sci. Rep.* **2015**, *5*, 8403.
[148] Y. Pei, Q. Chen, Y. C. Xiao, L. Liu, C. Y. Xua, L. Zhen, G. Henkelmanc, G. Cao, *Nano Energy* **2017**, *40*, 566.
[149] C. Delmas, C. Fouassier, P. Hagenmuller, *Physica B+C* **1980**, *99*, 81.
[150] C. Delmas, *Adv. Energy Mater.* **2018**, *8*, 1703137.
[151] K. Wang, Z. G. Wu, T. Zhang, Y. P. Deng, J. T. Li, X. D. Guo, B. B. Xu, B. H. Zhong, *Electrochim. Acta* **2016**, *216*, 51.
[152] R. Stoyanova, D. Carlier, M. Sendova-Vassileva, M. Yoncheva, E. Zhecheva, D. Nihtianova, C. Delmas, *J. Solid State Chem.* **2010**, *183*, 1372.
[153] X. Ma, H. Chen, G. Ceder, *J. Electrochem. Soc.* **2011**, *12*, A1307.
[154] J. Y. Hwang, S. T. Myung, Y. K. Sun, *Chem. Soc. Rev.* **2017**, *46*, 3529.
[155] P. F. Wang, H. Xin, T. T. Zuo, Q. Li, X. Yang, Y. X. Yin, X. Gao, X. Yu, Y. G. Guo, *Angew. Chem., Int. Ed.* **2018**, *57*, 8178.
[156] S. Komaba, N. Yabuuchi, T. Nakayama, A. Ogata, T. Ishikawa, I. Nakai, *Inorg. Chem.* **2012**, *51*, 6211.
[157] N. Yabuuchi, M. Kajiyama, J. Iwatate, H. Nishikawa, S. Hitomi, R. Okuyama, R. Usui, Y. Yamada, S. Komaba, *Nat. Mater.* **2012**, *11*, 512.
[158] D. Yuan, X. Hu, J. Qian, F. Pei, F. Wu, R. Mao, X. Ai, H. Yang, Y. Cao, *Electrochim. Acta* **2014**, *145*, 300.
[159] B. M. d. Boisse, D. Carlier, M. Guignard, C. Delmas, *J. Electrochem. Soc.* **2013**, *160*, A569.
[160] Y. Sun, S. Guo, H. Zhou, *Adv. Energy Mater.* **2018**, *451*, 1800212.
[161] Y. Xiao, P. F. Wang, Y. X. Yin, Y. F. Zhu, Y. B. Niu, X. D. Zhang, J. Zhang, X. Yu, X. D. Guo, B. H. Zhong, Y. G. Guo, *Adv. Mater.* **2018**, *30*, 1803765.
[162] L. Sun, Y. Xie, X. Z. Liao, H. Wang, G. Tan, Z. Chen, Y. Ren, J. Gim, W. Tang, Y. S. He, K. Amine, Z. F. Ma, *Small* **2018**, *14*, 1704523.
[163] W. G. Mumme, *Acta Cryst.* **1968**, *B21*, 1114.
[164] H. Kim, D. J. Kim, D.-H. Seo, M. S. Yeom, K. Kang, D. K. Kim, Y. Jung, *Chem. Mater.* **2012**, *24*, 1205.
[165] Y. Cao, L. Xiao, W. Wang, D. Choi, Z. Nie, J. Yu, L. V. Saraf, Z. Yang, J. Liu, *Adv. Mater.* **2011**, *23*, 3155.
[166] J. Yang, T. Yuan, B. Guo, C. Dai, Y. Liu, G. Li, G. Liu, M. Xu, *Chem. Commun.* **2017**, *53*, 9117.
[167] T. Y. Yu, J. Y. Hwang, D. Aurbach, Y. K. Sun, *ACS Appl. Mater. Interfaces* **2017**, *9*, 44534.
[168] S. Chong, Y. Wu, Y. Chen, S. Guo, Z. Tai, C. Shu, Q. Tan, J. Sun, Y. Liu, *Electrochim. Acta* **2019**, *293*, 299.
[169] J. Y. Hwang, S. M. Oh, S. T. Myung, K. Y. Chung, I. Belharouak, Y. K. Sun, *Nat. Commun.* **2015**, *6*, 6865.
[170] N. Yabuuchi, R. Hara, K. Kubota, J. Paulsen, S. Kumakura, S. Komab, *J. Mater. Chem. A* **2014**, *2*, 16851.
[171] X. Wu, G. L. Xu, G. Zhong, Z. Gong, M. J. McDonald, S. Zheng, R. Fu, Z. Chen, K. Amine, Y. Yang, *ACS Appl. Mater. Interfaces* **2016**, *8*, 22227.
[172] H. V. Ramasamy, K. Kaliyappan, R. Thangavel, V. Aravindan, K. Kang, D. U. Kim, Y. Park, X. Sun, Y.-S. Lee, *J. Mater. Chem. A* **2017**, *5*, 8408.
[173] S. Y. Xu, X. Y. Wu, Y. M. Li, Y. S. Hu, L. Q. Chen, *Chin. Phys. B* **2014**, *23*, 118202.
[174] S. M. Kang, J. H. Park, A. Jin, Y. H. Jung, J. Mun, Y. E. Sung, *ACS Appl. Mater. Interfaces* **2018**, *10*, 3562.
[175] U. Maitra, R. A. House, J. W. Somerville, N. Tapia-Ruiz, J. G. Lozano, N. Guerrini, R. Hao, K. Luo, L. Jin, M. A. Pérez-Osorio, F. Massel, D. M. Pickup, S. Ramos, X. Lu, D. E. McNally, A. V. Chadwick, F. Giustino, T. Schmitt, L. C. Duda, M. R. Roberts, P. G. Bruce, *Nat. Chem.* **2018**, *10*, 288.
[176] R. J. Clement, J. Billaud, A. R. Armstrong, G. Singh, T. Rojo, P. G. Bruce, C. P. Grey, *Energy Environ. Sci.* **2016**, *9*, 3240.
[177] Y. Liu, X. Fang, A. Zhang, C. Shen, Q. Liu, H. A. Enaya, C. Zhou, *Nano Energy* **2016**, *27*, 27.
[178] J. Alvarado, C. Ma, S. Wang, K. Nguyen, M. Kodur, Y. S. Meng, *ACS Appl. Mater. Interfaces* **2017**, *9*, 26707.
[179] S. Guo, Q. Li, P. Liu, M. Chen, H. Zhou, *Nat. Commun.* **2017**, *8*, 135.
[180] C. H. Jo, J. H. Jo, H. Yashiro, S. J. Kim, Y. K. Sun, S. T. Myung, *Adv. Energy Mater.* **2019**, *8*, 1702942.
[181] H. Ma, H. Su, K. Amine, X. Liu, S. Jaffer, T. Shang, L. Gu, H. Yu, *Nano Energy* **2018**, *43*, 1.
[182] E. Lee, J. Lu, Y. Ren, X. Luo, X. Zhang, J. Wen, D. Miller, A. DeWahl, S. Hackney, B. Key, D. Kim, M. D. Slater, C. S. Johnson, *Adv. Energy Mater.* **2014**, *4*, 1400458.
[183] S. Guo, P. Liu, H. Yu, Y. Zhu, M. Chen, M. Ishida, H. Zhou, *Angew. Chem., Int. Ed.* **2015**, *54*, 5894.
[184] Z. Y. Li, J. Zhang, R. Gao, H. Zhang, L. Zheng, Z. Hu, X. Liu, *J. Phys. Chem. C* **2016**, *120*, 9007.
[185] X. Qi, L. Liu, N. Song, F. Gao, K. Yang, Y. Lu, H. Yang, Y. S. Hu, Z. H. Cheng, L. Chen, *ACS Appl. Mater. Interfaces* **2017**, *9*, 40215.
[186] G. L. Xu, R. Amine, Y. F. Xu, J. Liu, J. Gim, T. Ma, Y. Ren, C. J. Sun, Y. Liu, X. Zhang, S. M. Heald, A. Solhy, I. Saadoune, W. L. Mattis, S.-G. Sun, Z. Chen, K. Amine, *Energy Environ. Sci.* **2017**, *10*, 1677.
[187] L. G. Chagas, D. Buchholz, C. Vaalma, L. Wuabc, S. Passerini, *J. Mater. Chem. A* **2014**, *2*, 20263.
[188] L. G. Chagas, D. Buchholz, L. Wu, B. Vortmann, S. Passerini, *J. Power Sources* **2014**, *247*, 377.

© 2019 WILEY-VCH Verlag GmbH & Co. KGaA, Weinheim

[189] X. Chen, X. Zhou, M. Hu, J. Liang, D. Wu, J. Wei, Z. Zhou, *J. Mater. Chem. A* **2015**, *3*, 20708.
[190] M. Keller, D. Buchholz, S. Passerini, *Adv. Energy Mater.* **2016**, *6*, 1501555.
[191] J. Zheng, P. Yan, W. H. Kan, C. Wang, A. Manthiram, *J. Electrochem. Soc.* **2016**, *163*, A584.
[192] C. Deng, P. Skinner, Y. Liu, M. Sun, W. Tong, C. Ma, M. L. Lau, R. Hunt, P. Barnes, J. Xu, H. Xiong, *Chem. Mater.* **2018**, *30*, 8145.
[193] D. W. Han, J. H. Ku, R. H. Kim, D. J. Yun, S. S. Lee, S. G. Doo, *ChemSusChem* **2014**, *7*, 1870.
[194] Z. G. Wu, J. T. Li, Y. J. Zhong, X. D. Guo, L. Huang, B. H. Zhong, D. A. Agyeman, J. M. Lim, D. H. Kim, M. H. Cho, Y. M. Kang, *ACS Appl. Mater. Interfaces* **2017**, *9*, 21267.
[195] H. Chen, H. Wu, Z. Zheng, T. Chen, X. Guo, J. Li, B. Zhong, *Electrochim. Acta* **2018**, *273*, 63.
[196] T. R. Chen, T. Sheng, Z. G. Wu, J. T. Li, E. H. Wang, C. J. Wu, H. T. Li, X. D. Guo, B. H. Zhong, L. Huang, S. G. Sun, *ACS Appl. Mater. Interfaces* **2018**, *10*, 10147.
[197] J. Qu, T. Sheng, Z. G. Wu, T. G. Chen, H. Chen, Z. G. Yang, X. D. Guo, J. T. Li, B. H. Zhong, X. S. Dou, *J. Mater. Chem. A* **2018**, *6*, 13934.
[198] G. Gao, D. Tie, H. Ma, H. Yu, S. Shi, B. Wang, S. Xu, L. Wang, Y. Zhao, *J. Mater. Chem. A* **2018**, *6*, 6675.
[199] Y. Xiao, P. F. Wang, Y. X. Yin, Y. F. Zhu, X. Yang, X. D. Zhang, Y. Wang, X. D. Guo, B. H. Zhong, Y. G. Guo, *Adv. Energy Mater.* **2018**, *8*, 1800492.

© 2019 WILEY-VCH Verlag GmbH & Co. KGaA, Weinheim